Journal of Medicinal Chemistry

pubs.acs.org/jmc

Article

Structural, Electronic, and Electrostatic Determinants for Inhibitor Binding to Subsites S1 and S2 in SARS-CoV-2 Main Protease

Daniel W. Kneller, Hui Li, Stephanie Galanie, Gwyndalyn Phillips, Audrey Labbé, Kevin L. Weiss, Qiu Zhang, Mark A. Arnould, Austin Clyde, Heng Ma, Arvind Ramanathan, Colleen B. Jonsson, Martha S. Head, Leighton Coates, John M. Louis, Peter V. Bonnesen,* and Andrey Kovalevsky*

Cite This: https://doi.org/10.1021/acs.jmedchem.1c01475

Read Online

ACCESS | Metrics & More | Article Recommendations | Supporting Information

ABSTRACT: Creating small-molecule antivirals specific for severe acute respiratory syndrome coronavirus 2 (SARS-CoV-2) proteins is crucial to battle coronavirus disease 2019 (COVID-19). SARS-CoV-2 main protease (M^{pro}) is an established drug target for the design of protease inhibitors. We performed a structure−activity relationship (SAR) study of noncovalent compounds that bind in the enzyme's substrate-binding subsites S1 and S2, revealing structural, electronic, and electrostatic determinants of these sites. The study was guided by the X-ray/neutron structure of M^{pro} complexed with Mcule-5948770040 (compound **1**), in which protonation states were directly visualized. Virtual reality-assisted structure analysis and small-molecule building were employed to generate analogues of **1**. *In vitro* enzyme inhibition assays and room-temperature X-ray structures demonstrated the effect of chemical modifications on M^{pro} inhibition, showing that (1) maintaining correct geometry of an inhibitor's P1 group is essential to preserve the hydrogen bond with the protonated His163; (2) a positively charged linker is preferred; and (3) subsite S2 prefers nonbulky modestly electronegative groups.

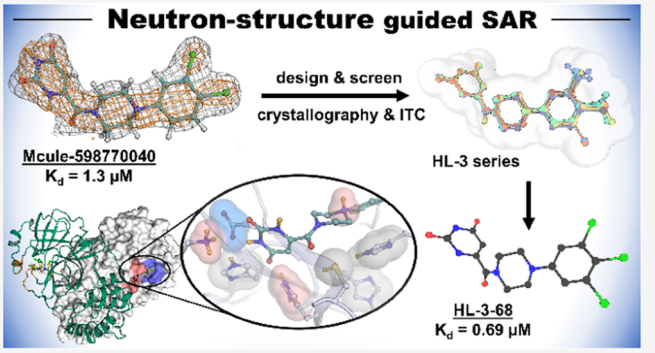

INTRODUCTION

Since the start of the coronavirus disease 2019 (COVID-19) pandemic in early 2020, several preventative and treatment options have been developed, including several vaccines and antiviral therapies.[1−4] The COVID-19 vaccines developed in record time are now potentially saving millions of lives. However, due to vaccine hesitancy, pre-existing health conditions, and vaccine escape variants of severe acute respiratory syndrome coronavirus 2 (SARS-CoV-2),[5] a significant proportion of the population will remain at risk, creating an urgent priority to advance existing therapeutics. COVID-19 is caused by a novel coronavirus, SARS-CoV-2, believed to be of zoonotic origin,[6,7] raising concerns that other easily transmissible respiratory viruses will emerge to cause future pandemics. The arsenal of therapeutic intervention options will undoubtedly be expanded by designing multiple small-molecule drugs that inhibit various viral targets disrupting essential steps in the SARS-CoV-2 replication cycle.[8] This bolstered preparedness strategy has the potential to yield broad-spectrum antivirals providing a means of tackling future pathogenic coronaviruses.

3-Chymotrypsin-like protease ($3CL^{pro}$), also known as the main protease (M^{pro}), from SARS-CoV-2 is a viral cysteine protease enzyme[9] and an important drug target that has attracted considerable attention from structural and computational biologists and drug designers.[10−15] SARS-CoV-2 is a single-stranded, positive-sense RNA virus with a genome of ∼30k nucleotides resembling mRNA.[16] Host cell ribosomes partially translate the genomic mRNA to generate two polyproteins, pp1a and pp1ab, encoded by the viral replicase gene during the initial steps of the virus replication cycle.[16,17] The proteolytic cleavage of pp1a and pp1ab is vital for SARS-CoV-2 proliferation and liberates 16 individual viral protein components necessary for the viral genome transcription activity. This essential step in the SARS-CoV-2 replication cycle is accomplished by M^{pro}, and another cysteine protease, the papain-like protease (PL^{pro}), through hydrolyzing peptide bonds within the two polyproteins at specific locations. Small-molecule inhibitors of the viral protease enzymatic activity have strong clinical precedence for blocking virus replication, and hence, the fervent interest of the scientific community to develop coronavirus-specific protease inhibitors. The active site of M^{pro} is distinct from the known human proteases; thus, off-

Received: August 20, 2021

target binding of specific M^{pro} inhibitors can be minimized.[10,11] Conversely, conservation of the M^{pro} active site across various coronaviruses creates an opportunity to design pan-coronavirus antivirals.[18]

Significant effort in the design of M^{pro} inhibitors against SARS-CoV-2[8,19−21] has focused on the reversible and irreversible (suicidal) covalent inhibitors, including compounds initially designed for the inhibition of SARS-CoV M^{pro}.[22−25] Such inhibitors contain chemical groups, or warheads, that are reactive toward the catalytic cysteine of M^{pro}, Cys145. The hepatitis C virus clinical protease inhibitor boceprevir and the feline peritonitis virus protease inhibitor GC-376 were initially considered for drug repurposing, leading to the rational design of hybrid inhibitors.[26−28] In addition, noncovalent competitive and allosteric inhibitors have captured interest due to the availability of high-throughput virtual and experimental screening of large compound libraries that leverage new advances in supercomputing and fast X-ray crystallographic screening.[15,29−32] Compounds can be fed into structure-based drug design pipelines and chemically modified to improve their potency to inhibit SARS-CoV-2 M^{pro}.[33−36] Moreover, noncovalent inhibitors may have a higher selectivity for M^{pro} compared to covalent compounds that can also target host proteases and can possess elevated cytotoxicity due to binding to other human proteins.[33,36]

The active site of M^{pro} consists of subsites S5−S1′, which can accommodate substrate and inhibitor groups at positions P5−P1′. Subsites S1 and S2 are selective for Gln and a medium-sized hydrophobic residue like Leu or Phe, respectively.[11,37−39] A recent study analyzed the effect of chemical modifications in a noncovalent inhibitor ML188 on its binding to M^{pro}.[36] Here, we report a structure−activity relationship (SAR) study performed on a competitive noncovalent inhibitor Mcule-5948770040 (compound **1**) of a novel scaffold that we recently discovered through a large-scale virtual screening and validated using *in vitro* enzyme inhibition assays and X-ray crystallography.[40] The aim of our SAR study was to chemically modify compound **1** that binds across the M^{pro} catalytic site in the substrate-binding subsites S1 and S2 to reveal structural, electronic, and electrostatic determinants of these ligand-binding sites. Compound **1** has a general architecture of P1−linker−P2 (Scheme 1). We initiated the study by obtaining a joint X-ray/neutron (XN) structure of the M^{pro}-**1** complex at near-physiological temperature and neutral pH (Figure 1a). The XN structure permitted us to fully map the hydrogen positions (observed as deuterium atoms) in the M^{pro} active site and compound **1**, accurately determining protonation states of the enzyme amino acid residues and the inhibitor. With this information in hand, we systematically derivatized P1, P2, and linker groups producing a series of compounds; named as the HL-3 series (Scheme 1). A virtual reality-assisted structure analysis and small-molecule building were employed to generate derivatives of **1**, considering the geometric constraints of the M^{pro} subsites S1 and S2 and the feasibility of the syntheses. *In vitro* enzyme inhibition assays demonstrated the effect of chemical modifications on the ability of the modified compounds to inhibit M^{pro}. In contrast, subsequent X-ray crystallographic analysis at room temperature identified the structural determinants for P1, P2, and linker binding. Moreover, we designed an improved inhibitor, compound HL-3-68, that showed several-fold better inhibition of M^{pro} *in vitro*.

Scheme 1. Chemical Diagrams of Mcule-5948770040 (Compound 1) and Its Derivatives[a]

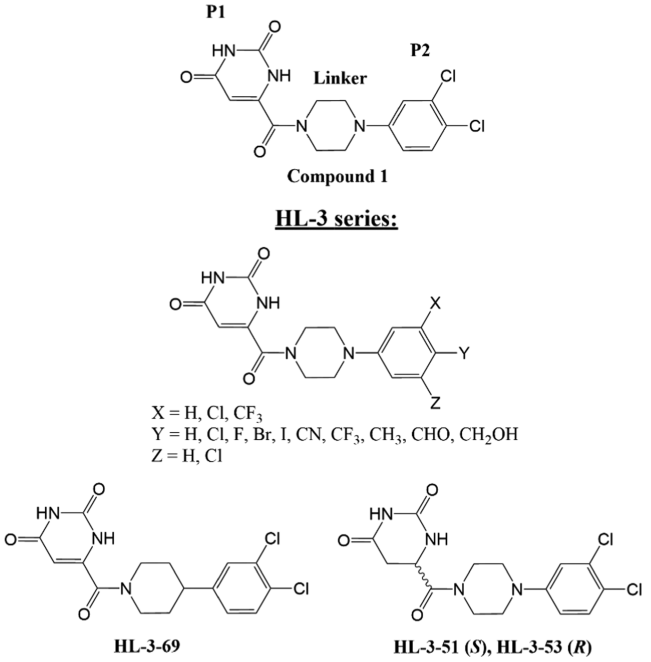

[a]For the generalized structure of the HL-3 series not all possible combinations of X, Y, and Z substituents were examined. The full list of HL-3 series of compounds, including their chemical structures, is given in Table S1.

RESULTS

Protonation States in the M^{pro}-1 Complex. Neutron crystallography of the M^{pro}-**1** complex was employed to accurately resolve the positions of hydrogen atoms in the active site of M^{pro} and compound **1**. Neutron and X-ray diffraction datasets to 2.5 and 2.2 Å resolutions, respectively, were collected at room temperature and neutral pH from a large deuterated protein crystal and then jointly refined to produce accurate positions of both deuterium and heavy atoms (Table S1). Henceforth, the analysis includes comparisons to previously determined neutron structures of ligand-free M^{pro}[41] and M^{pro} bound to the covalent α-ketoamide inhibitor telaprevir.[42] Compound **1** (Figure 1b) was modeled into the electron and nuclear density maps with high confidence (Figure 1c). For hydrogen bonds, distances between a deuterium (D) atom and the heavy atom are reported henceforth.

Direct interactions between M^{pro} and the P1 and P2 groups of **1** are shown in Figure 2a with $2F_o - F_c$ and D-omit $F_o - F_c$ nuclear density maps. The uracil-like P1 group of **1** contains a carbonyl that forms a short 1.7 Å hydrogen bond with a doubly protonated His163. This carbonyl's second lone pair of electrons makes a weaker unconventional C−H···O hydrogen bond with Cδ2 of His172. The other carbonyl of the P1 group forms a D_2O-mediated interaction with Ser1′ of the second M^{pro} protomer. Another D_2O-mediated interaction to Asn142 arises from the amide ND group at the P1 group's 2 position, whereas the amide ND at the 4-position forms a 2.0 Å hydrogen bond with the carboxylate side chain of Glu166. To facilitate this interaction, the Glu166 carboxylate rotates from its position observed in the ligand-free M^{pro} structure toward **1**, and His163 gains a D atom on Nε2 to become positively

https://doi.org/10.1021/acs.jmedchem.1c01475
J. Med. Chem. XXXX, XXX, XXX−XXX

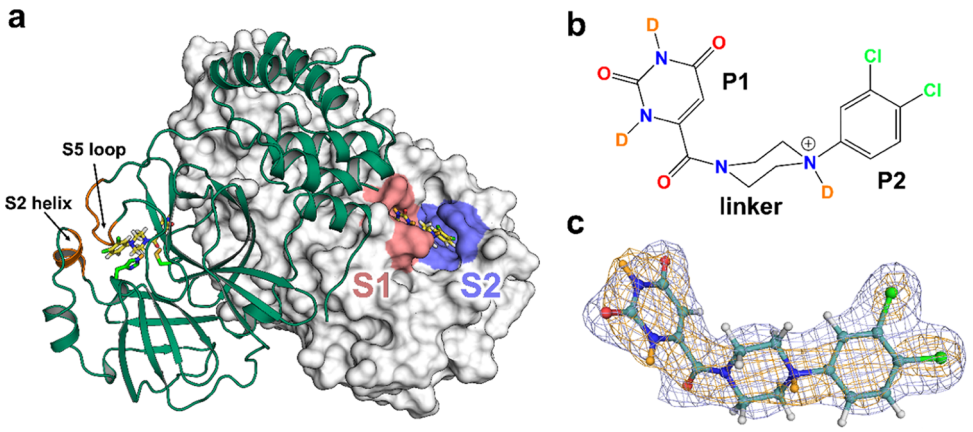

Figure 1. Compound **1** binds to the S1 and S2 subsites of M^{pro}. (a) Dimer of M^{pro}-**1** is represented with one protomer as cartoon (green) and the other as surface (white). The locations of subsites S1 (pink) and S2 (purple) are highlighted. The S2 helix and S5 loop are labeled in orange. The Cys145 and His41 catalytic dyad are shown as sticks. PDB ID 7N8C. (b) Chemical structure of compound **1** as observed in M^{pro}-**1**. (c) Compound **1** from M^{pro}-**1** shown in a ball-and-stick representation (teal carbons). H/D-exchanged D atoms are colored in orange. The electron density $2F_o - F_c$ map (blue mesh) and nuclear density $2F_o - F_c$ map (orange mesh) contoured to 1σ.

charged in M^{pro}-**1** (Figure S1a). Interestingly, the same conformational change of the Glu166 side chain was observed in the telaprevir-bound neutron structure, where His163 was also found in the doubly protonated state, relative to the ligand-free M^{pro} (Figure S1b). However, telaprevir possesses a short hydrophobic norvaline P1 group that prevents a direct polar interaction with the enzyme; instead, a water molecule is recruited to this position to hydrogen bond with His163. The aromatic dichlorobenzene P2 group orchestrates itself into the hydrophobic S2 subsite by displacing Met49 and S2 helix (residues 46−52) and rearranging His41 and Gln189 to create $\pi-\pi$ stacking interactions.[40] P1 and P2 groups of **1** are connected by a saturated heterocyclic piperazine−amide linker that includes a carbonyl aimed toward the oxyanion hole and a potentially ionizable tertiary amine preceding P2. Analysis of the nuclear density demonstrated that the latter amine nitrogen is protonated with the D atom directed away from His41 and into the bulk solvent. As a result, compound **1** is a cation with a +1 positive charge.

The catalytic site of M^{pro} is composed of a noncanonical catalytic dyad, Cys145 and His41, thought to be assisted by a highly coordinated conserved water molecule (D_2O_{cat}). The catalytic dyad exists in the zwitterionic state in ligand-free M^{pro} as discrete anionic thiolate and cationic imidazolium side chains.[41] The hydrogen-bonding landscapes of His41 and D_2O_{cat} in M^{pro}-**1** are presented in Figure 2b. In this complex, the catalytic dyad is neutralized with Cys145 observed as a thiol (-SD), and His41 singly protonated on Nε2 but not on Nδ1. The Cys145 thiol deuterium was refined to ∼85% D occupancy. Relative to the ligand-free M^{pro} and M^{pro}-telaprevir neutron structures, the His41 side chain is flipped about 180°, its position in M^{pro}-**1** being stabilized by a new hydrogen bond formed between Nε2-D and the His164 main chain carbonyl (Figures 2c and S1b). Consequently, a conserved hydrogen bond with D_2O_{cat} observed in the other two neutron structures is eliminated to create a new hydrogen bond made by the Nδ1 with a D_2O molecule recruited from the bulk solvent.

D_2O_{cat} in M^{pro}-**1** is oriented by donating its D atoms in hydrogen bonds with the His164 and Asp187 side chains in a rotation pose not seen in either the ligand-free or telaprevir-bound neutron structures (Figure S1a,b). In contrast to ligand-free M^{pro} in which His164 is doubly protonated, His164 is neutrally charged in M^{pro}-**1**, possessing strong nuclear density for Nδ1-D that is hydrogen-bonded to Thr175 (Figure 2b). Moreover, this neutral protonation state configuration of His164 is different from that observed in the M^{pro}-telaprevir neutron structure where Nε2 is protonated, and the hydrogen bond to Thr175 is absent. Thus, in M^{pro}-**1**, D_2O_{cat} rotates to donate its D atoms in hydrogen bonds with His164 Nε2 and Asp187 carboxylate.

Design of Compound 1 Derivatives: HL-3 Series. The architecture of compound **1** can be divided into three parts: P1 and P2 groups and the linker (Scheme 1 and Figure 1b). P1 is a uracil-like, 6-pyrimidine-2,4(1*H*,3*H*)-dione, substituent capable of direct hydrogen bonding with M^{pro} residues His163 and Glu166 in the S1 subsite. The linker is a piperazine-1-carbonyl moiety whose carbonyl group is anchored by the oxyanion hole of the catalytic site. P2, a substituted benzene substituent, inserts into the mostly hydrophobic S2 subsite bordered by Met49 from the S2 helix, main chain atoms of Arg188 and Gln189, and side chains of His41, Cys44, Tyr54, and Gln189. The Tyr54 phenolic hydroxyl is the only group that potentially can play a role of a hydrogen-bonding partner with a P2 group of an inhibitor. To improve inhibitor affinity and probe the chemical determinants for ligand binding to S1 and S2, we designed an array of compound **1** derivatives, which we call HL-3 series, to methodically assess how the P1, linker, and P2 groups contribute to M^{pro} inhibition.

Our design strategy of compound **1** derivatives, *i.e.*, HL-3 compounds (Scheme 1 and Table 1), included chemical modifications to each of its three parts, taking into consideration specific geometric and hydrogen-bonding constraints of S1 and S2 subsites and the feasibility of syntheses for designed compounds. We employed virtual reality software to immerse into the M^{pro} structure, to modify the scaffold of compound **1**, and to perform structural analysis of the modeled complexes. First, we examined the effect of saturating the olefinic portion of the uracil-like (pyrimidine-2,4(1*H*,3*H*)-dione) P1 group that creates a nonplanar sp^3-hybridized endocyclic carbon. Both enantiomers were made to mimic the γ-lactam ring commonly used as inhibitor's P1 (HL-3-51, HL-3-53). Such modification should not eliminate the P1 group's ability to hydrogen bond with His163, which is a prerequisite for M^{pro} inhibitors. Next, we examined the effect

https://doi.org/10.1021/acs.jmedchem.1c01475
J. Med. Chem. XXXX, XXX, XXX−XXX

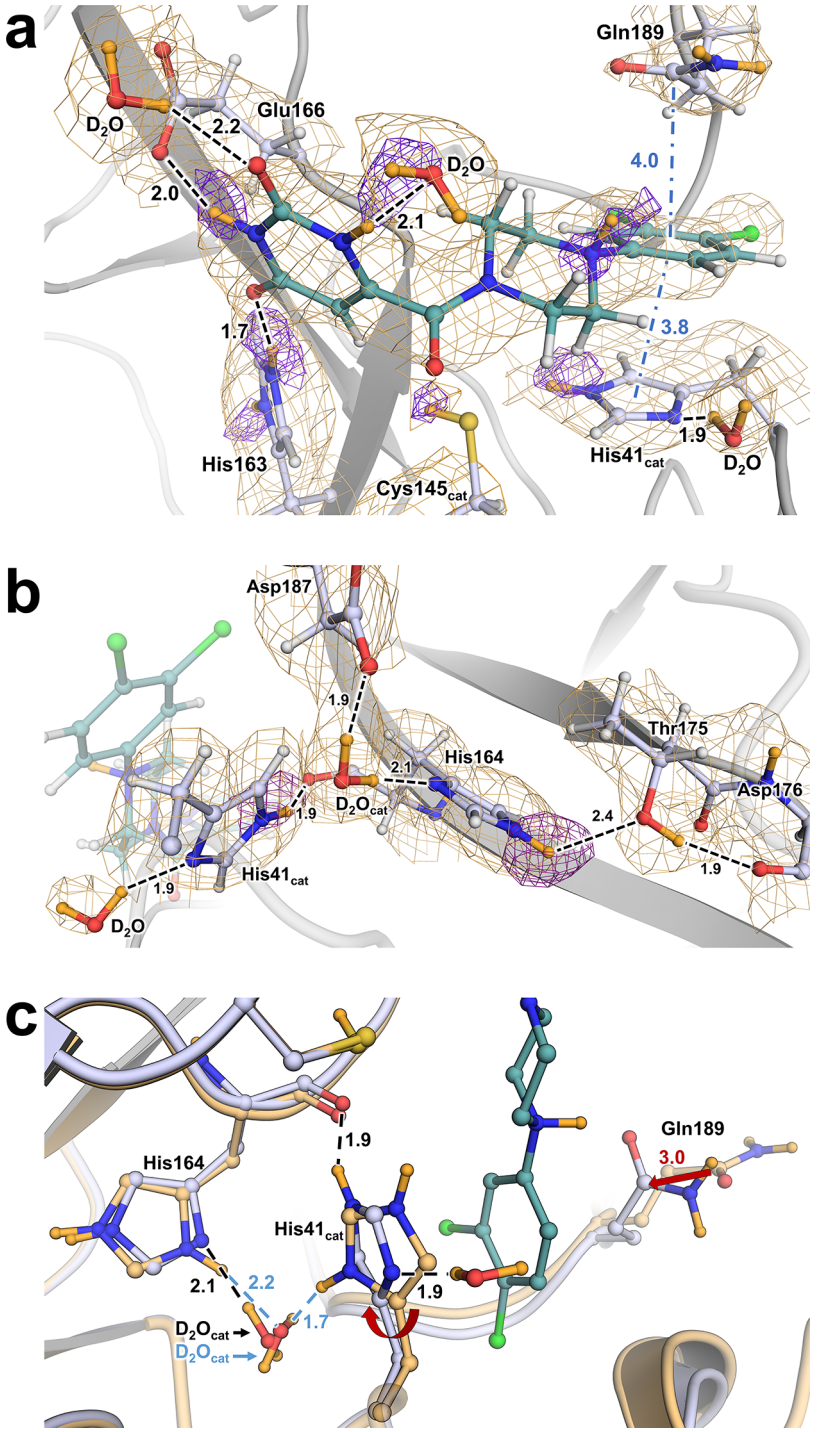

Figure 2. Atomic details of the SARS-CoV-2 M^{pro} complex with compound **1** determined by X-ray/neutron crystallography. (a) M^{pro} protonation states and molecular interactions with **1**. Protein structures are presented as cartoon with side chains and the ligand in ball-and-stick representation. H-bonds are represented as dashes, while π-interactions are represented as blue dash-dots. Distances are in angstrom. The $2F_o - F_c$ nuclear density map as an orange mesh is contoured at 1σ. Omit maps for D atoms are shown as a purple mesh and contour levels are adjusted for clarity as follows: linker amine D is 2.0σ, P1 amine Ds is 3.0σ, His41 Nε2 D is 2.5σ, His163 Nδ1 D is 4.0σ, and Nε2 D is 3.0σ. (b) H-bond network of the catalytic D_2O and His41 side chain. The $2F_o - F_c$ nuclear density map as an orange mesh is contoured at 1.5σ. The omit map for His164 Nδ1 D is contoured at 3.0σ. (c) Superposition of M^{pro}-**1** (blue carbons) and M^{pro} ligand-free (light orange carbons, PDB code 7JUN) showing His41 flip and Gln189 shift in the complex. Red arrows indicate conformational shifts from ligand-free to compound **1** complex. Ligand-free is labeled in blue where different. Superposition calculated by least-squares fitting on Cα atoms.

of removing a positive charge from the linker, where the aniline nitrogen is observed in the protonated quaternary ammonium state in our neutron structure. To achieve this, the aniline nitrogen was replaced with a saturated carbon by substitution of a piperidine moiety for the piperazine in the linker (HL-3-69). The most extensive modifications were made to the P2 group by varying substituents at positions 3, 4, and 5 of the phenyl ring. We examined the effect of removing one Cl from

https://doi.org/10.1021/acs.jmedchem.1c01475
J. Med. Chem. XXXX, XXX, XXX−XXX

Table 1. 50% Inhibitory Concentration (IC_{50}) Values for the Inhibition of SARS-CoV-2 M^{pro} by a Series of HL-3 Compounds[ac]

Compound	Chemical Structure	IC50, μM	PDB ID
Compound **1** (Mcule-5948770040)	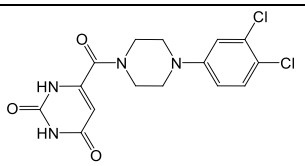	0.68 [0.48, 0.97][b,40]	7LTJ
HL-3-68	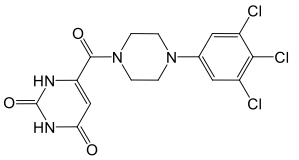	0.29 [0.22, 0.40]	7RLS
Mcule-CSR-494190-S1	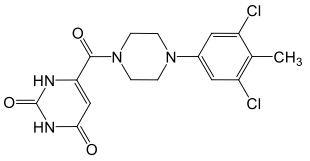	0.29 [0.19, 0.43]	7RM2
HL-3-78	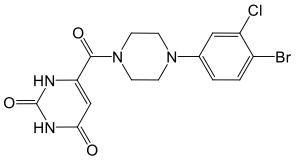	0.61 [0.37, 0.96]	7RMB
HL-3-52	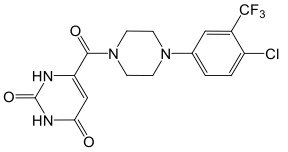	1.4 [0.80, 2.3]	7RME
HL-3-87	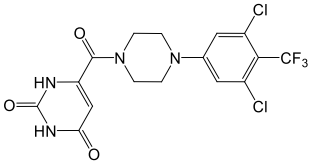	1.4 [0.9, 2.2]	N/D[c]
HL-3-70	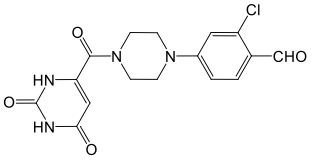	6.2 [4.8, 8.0]	7RMT
HL-3-63	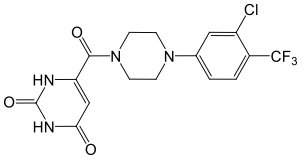	6.4 [4.3, 9.5]	7RMZ
HL-3-69	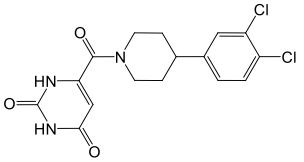	8.8 [6.3, 13]	7RN4
HL-3-45	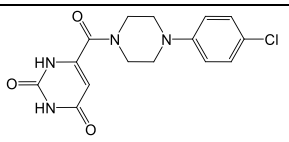	> 20	7RNH

https://doi.org/10.1021/acs.jmedchem.1c01475
J. Med. Chem. XXXX, XXX, XXX−XXX

Table 1. continued

Compound	Chemical Structure	IC50, μM	PDB ID
HL-3-71	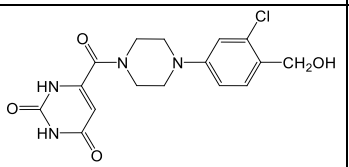	> 20	7RNK
HL-3-46	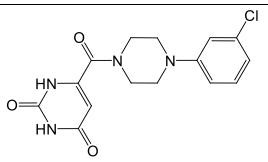	> 20	N/D
HL-3-43	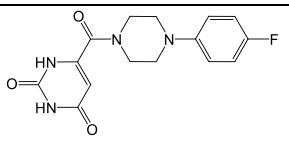	> 20	N/D
HL-3-44	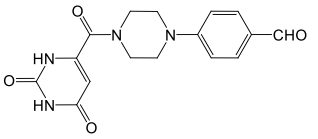	> 20	N/D
HL-3-49	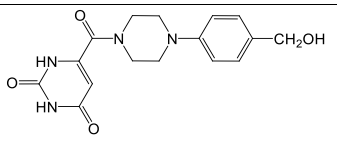	> 20	N/D
HL-3-62	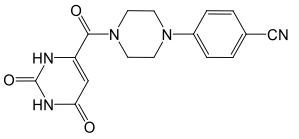	> 20	N/D
HL-3-50	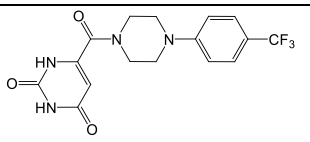	> 20	N/D
HL-3-51 HL-3-53	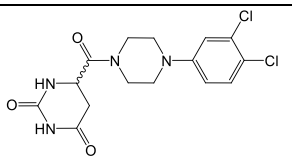	> 20	N/D
HL-3-65	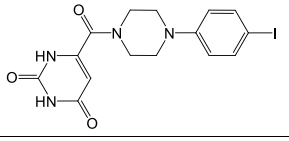	> 20	N/D

[a]X-ray crystallographic statistics for the obtained structures is given in Table S2. [b]95% confidence interval (CI). [c]N/D—not determined.

either position 3 or 4 and synthesized singly substituted derivatives at position 4 containing groups such as F, I, CN, CF_3, CHO (aldehyde), and CH_2OH. In addition, we retained Cl in position 3 and varied substituents in position 4 to include Br, CF_3, CHO, and CH_2OH. In another compound, Cl in position 4 remained, but position 3 contained a CF_3 group. Finally, we investigated derivatives with three substituents in positions 3, 4, and 5. In this series, the 3,5-*meta* positions had Cl groups, whereas *para* position 4 consisted of Cl, CF_3, or CH_3.

Various halides (F, Cl, I), nitrile, and trifluoromethyl were examined at the *para* position to modulate the electronic properties of the P2 group. In contrast, aldehyde and hydroxymethyl substituents were investigated to determine whether the Tyr54 side chain can act as a hydrogen-bond partner, donor or acceptor. Sterically bulkier substituents were not considered for synthesis due to geometric constraints of the S2 subsite.

Inhibition of M^{pro} by HL-3 Compounds. To determine the effect of the chemical modifications within the HL-3 series of compounds on their ability to inhibit M^{pro} compared to compound **1**, an initial M^{pro} activity inhibition screen was performed at a 20 μM inhibitor concentration. Eight compounds showed at least 50% M^{pro} activity inhibition at

https://doi.org/10.1021/acs.jmedchem.1c01475
J. Med. Chem. XXXX, XXX, XXX−XXX

Table 2. Binding Affinities of Compound 1 and Selected Inhibitors Determined by *In Vitro* Assays (K_i) and Isothermal Titration Calorimetry (ITC) (K_d and Thermodynamic Parameters ΔH, ΔS, and ΔG of Binding)

Compound	Chemical Structure	K_i, μM	K_d, μM	Stoichiometry, N	ΔH, kcal/mol	ΔS, cal/mol·K	ΔG, kcal/mol
Compound **1** Mcule-5948770040	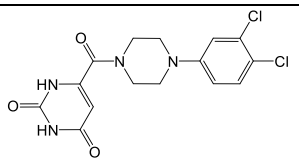	2.9 [2.2, 4.0][40]	1.30±0.18	0.96±0.01	-8.32±0.17	-0.70	-8.11
HL-3-68	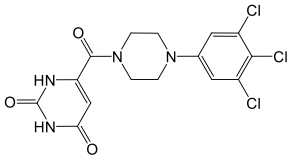	0.89 [0.72, 1.1]	0.69±0.21	0.90±0.02	-7.75±0.27	2.40	-8.47
Mcule-CSR-494190-S1	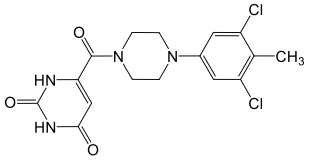	1.4 [1.1, 1.7]	1.32±0.29	0.97±0.02	-9.10±0.28	-3.16	-8.15

20 μM (Table 1) and were further characterized by assaying inhibition across a range of concentrations to determine 50% inhibitory concentration (IC_{50}) values (eq 1). The rest of the compounds were excluded from further measurements because their IC_{50} values were well above 20 μM. Compound **1** produced an IC_{50} of 0.68 μM in the current experiments (Table 1).

Replacing P1 uracil-like group with either of dihydropyrimidine-2,4(1*H*,3*H*)-dione enantiomers (HL-3-51 and HL-3-53) had a considerable effect, with the IC_{50} values being above 20 μM for the two derivatives. Therefore, the structurally conserved S1 subsite cannot accommodate the bent structures of these P1 groups. Interestingly, replacing the protonated positively charged aniline nitrogen with carbon to give HL-3-69 also negatively affected the compound's potency (IC_{50} = 8.8 μM), even though this nitrogen does not make close contacts with M^{pro} residues. Hence, it appears that more than an order of magnitude increase in IC_{50} for HL-3-69 compared to compound **1** can be attributed to the altered electrostatics of the inhibitor.

The removal of the Cl substituent at the 3-position of the P2 group to generate the monosubstituted derivative HL-3-45, and then substituting Cl at the 4-position with various groups, such as F, I, CHO, CH_2OH, CN, and CF_3, leads to dramatic losses of these derivatives' potencies. A similar result was obtained for compounds HL-3-46 and HL-3-71, in which the chlorine at the 4-position is replaced, respectively, with −H or $-CH_2OH$. These observations clearly indicated that −Cl at the 3-position of the P2 group is essential for a compound to maintain its potency. Indeed, adding Cl back to the 3-position for monosubstituted compounds with CHO (HL-3-44) or CF_3 (HL-3-50) at the 4-position significantly restored potency, with HL-3-70 and HL-3-63 possessing IC_{50} values of of 6.2 and 6.4 μM, respectively. However, the potencies of HL-3-70 and HL-3-63 are an order of magnitude worse than that of compound **1**, indicating that the presence of sterically larger and more electronegative substituents than Cl at the 4-position reduces an inhibitor's potency. Replacing Cl at the 4-position with −Br, whose van der Waals radius of 1.97 Å is slightly larger than that of Cl (1.90 Å) and electronegativity lower than that of Cl, while maintaining Cl at the 3-position, resulted in compound HL-3-78, which demonstrated potency as good as compound **1**. Unexpectedly, we determined that when Cl and CF_3 in HL-3-63 swap positions to give HL-3-52, the IC_{50} improves several folds to 1.4 μM, which is only about twice as high as that for compound **1**. Adding an extra Cl substituent to HL-3-63 at the 5-position (HL-3-87) caused a similar reduction in IC_{50}. The latter two observations demonstrated that the 3-position of the P2 group could accommodate a bulkier and more electronegative substituent, and addition of Cl to the 5-position on the benzene ring is beneficial for an inhibitor's potency.

With this in mind, we analyzed the potencies of two molecules, HL-3-68 and Mcule-CSR-494190-S1, with −Cl in positions 3 and 5 and either Cl or CH_3 at position 4, respectively (Table 2). Both showed improved inhibition potency relative to compound **1**, indicating the preference of the S2 subsite for less bulky substituents with moderate-to-low electronegativity. We thus determined K_i values for HL-3-68 and Mcule-CSR-494190-S1 from the initial rates determined across a range of inhibitor and substrate concentrations (eq 2). K_i measurements confirmed that the inhibitor HL-3-68 had the highest affinity, with a sub-μM K_i of 0.89 μM, followed by Mcule-CSR-494190-S1 with a K_i of 1.4 μM. The significant accuracy of K_i measurements indicates that the potencies of HL-3-68 and Mcule-CSR-494190-S1 are 3-fold and 2-fold better than the K_i of 2.9 μM of the previously reported compound **1**.[40] Of note, none of the compounds demonstrated antiviral activities against SARS-CoV-2 in cell-based assays (Figure S2).

Isothermal Titration Calorimetry (ITC). To directly assess the thermodynamic binding properties of compound **1** and the two most potent inhibitors HL-3-68 and Mcule-CSR-494190-S1, we performed isothermal titration calorimetry (ITC, Table 2 and Figure S3). The K_d values measured by ITC are in good agreement with the K_i values obtained by enzyme kinetics. HL-3-68 demonstrates sub-μM affinity to M^{pro}, binding ∼2-fold better to the enzyme than the other two compounds. The binding of all three compounds to M^{pro} is driven primarily by enthalpy. Compound **1** binds to the

https://doi.org/10.1021/acs.jmedchem.1c01475
J. Med. Chem. XXXX, XXX, XXX−XXX

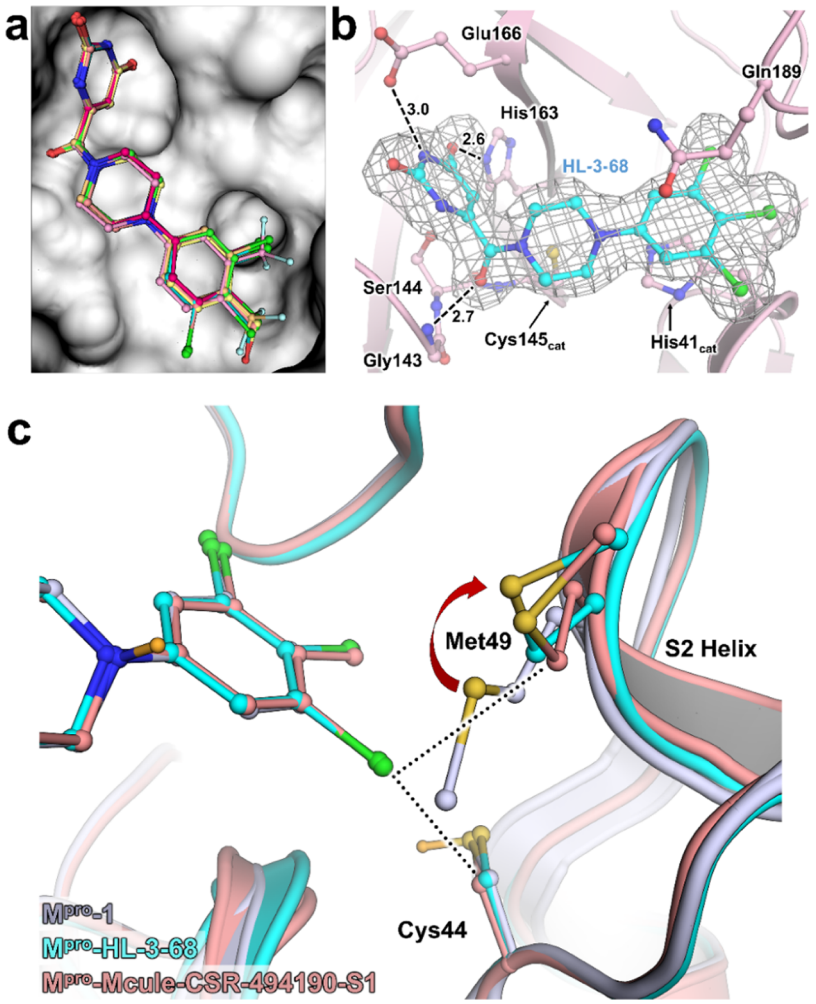

Figure 3. M^{pro} inhibition by HL-3 compounds. (a) Binding modes of nine HL-3 compounds co-crystallized with M^{pro}. (b) HL-3-68 (cyan) bound in the active site of M^{pro} (pink). Electron density omit $F_o - F_c$ map (gray mesh) is contoured at 3σ. H-bonds are shown as black dashes. Distances are in angstrom. PDB ID 7RLS. (c) Superposition of M^{pro}-**1** X-ray/neutron structure (PDB ID 7N8C) with HL-3-68 (PDB ID 7RLS) and Mcule-CSR-494190-S1 (PDB ID 7RM2) complex X-ray structures showing rotation of Met49 to accommodate the Cl at 5-position of the aromatic P2 group. Van der Waals contacts for improved inhibitors represented as dotted lines. Superposition was calculated by least-squares fitting on Cα atoms.

enzyme with essentially no change in entropy, whereas ΔS of binding for Mcule-CSR-494190-S1, although small (−3.16 cal/(mol·K)), is negative and therefore contributes unfavorably to the binding with $-T\Delta S$ of +0.95 kcal/mol. Conversely, substitution of the methyl at the 4-position of the P2 group with Cl reverts ΔS to a small positive value of 2.4 cal/(mol·K). Interestingly, ΔH of binding is the most favorable for Mcule-CSR-494190-S1, although its ΔS is the most unfavorable. The interplay of the enthalpy and entropy components results in HL-3-68 possessing the highest affinity for M^{pro} (K_d = 0.69 μM).

Room-Temperature X-ray Structures of M^{pro} in Complex with HL-3 Compounds. To shed light on the SAR between M^{pro} and HL-3 compounds, we obtained nine room-temperature X-ray structures of M^{pro} co-crystallized with selected HL-3 compounds at resolutions in the range of 1.85−2.10 Å (Table S2 and Figure S4). We did not obtain the crystal structures of M^{pro} complexes with other compounds because they were either significantly less potent than compound **1** or their complexes did not crystallize. Comparisons of these structures with M^{pro}-**1** provide insights into how substitutions at positions 3, 4, and 5 of the aromatic P2 group alter the binding of HL-3 compounds and correlate with their inhibition potencies. Inhibitors of all determined structures bind in identical fashion (Figure 3a) anchored to M^{pro} by invariant hydrogen bonds (2.6 ± 0.1 Å between the heavy atoms) of the uracil P1 group with His163 and the linker's carbonyl with the main chain amide nitrogen of Gly143. Some shifts in the positions of the aromatic P2 group up to 0.5 Å are observed due to the various substituents in positions 3, 4, and 5.

M^{pro}-HL-3-68 (Figure 3b) and M^{pro}-Mcule-CSR-494190-S1 superimpose with the M^{pro}-**1** joint X-ray/neutron structure with Cα RMSD values in the range of 0.2−0.23 Å. Substituting Cl or CH_3 at the 4-position of the P2 probes the effect of the chemical group's hydrophobicity at the S2 site with a small difference in van der Waals radii. Increased hydrophobicity of the CH_3 group in M^{pro}-Mcule-CSR-494190-S1 compared to Cl in M^{pro}-HL-3-68 translates structurally only into the nearby Pro52 ring that adopts the exo-conformation instead of the endo geometry, respectively. Pro52 terminates the short S2 α-helix spanning residues 46−52, where the Met49 side chain acts to gate the S2 subsite. The effect on the S2 subsite arising from −Cl at the P2 5-position can be observed here through superpositions of the M^{pro}-**1** neutron structure with the M^{pro}-

https://doi.org/10.1021/acs.jmedchem.1c01475
J. Med. Chem. XXXX, XXX, XXX−XXX

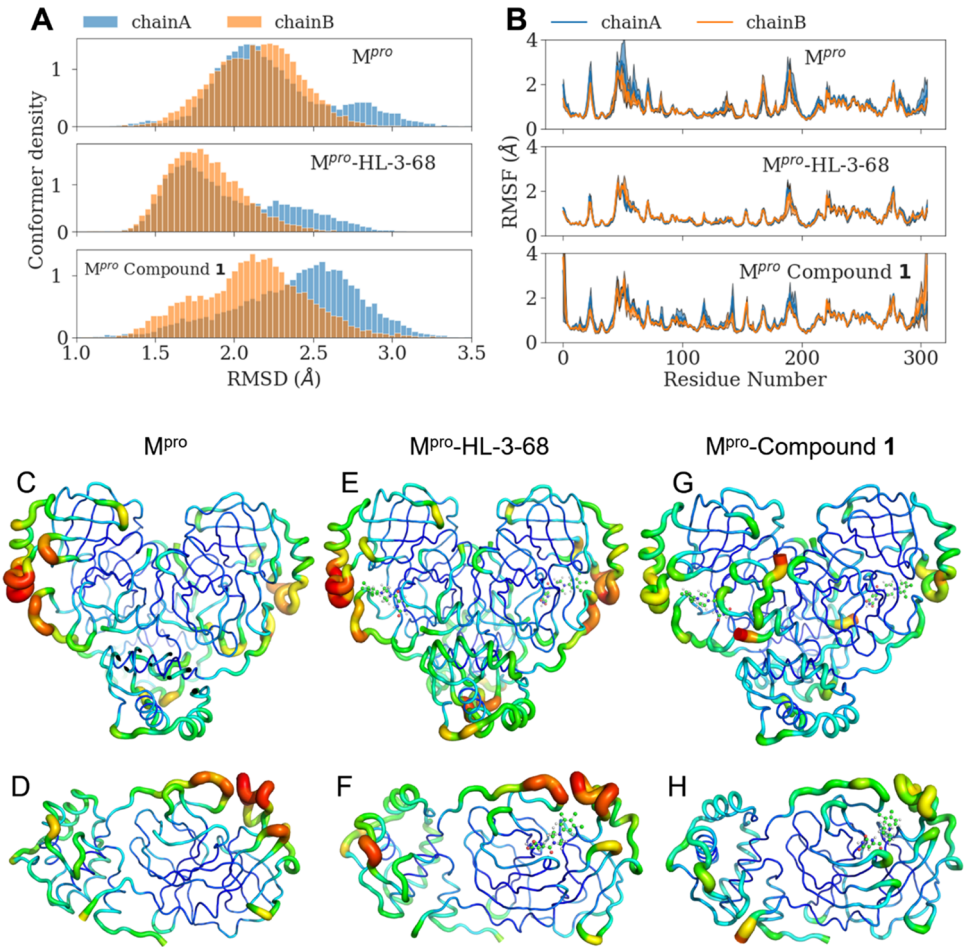

Figure 4. Root-mean-square analysis of MD trajectories. (A) Distribution of the root-mean-square deviations (RMSD) captured as a histogram over the course of MD simulations from the three replicas showing that chain A exhibits higher fluctuations than chain B in the ligand-free state (top panel). In the ligand-bound states, the asymmetric nature of fluctuations is still present; however, M^{pro}-HL-3-68 (middle panel) exhibits a considerably lower degree of fluctuations compared to M^{pro} compound **1** (bottom panel) as a consequence of the increased stability of the interactions within the primary binding site. The starting model was PDB ID 7JUN for apo-M^{pro} simulation, 7RLS for the HL-3-68 complex, and 7N8C for the complex with compound **1**. (B) Root-mean-square fluctuations (RMSFs) of the individual chains captured across the three sets of replicas further reinforce the observation that both ligands stabilize the M^{pro}-binding site. The shaded regions highlight the variation across three independent replicas of the simulations (for each system). (C) Putty-like representation of the RMSF of the ligand-free M^{pro} dimer simulations depicts large-scale fluctuations along the primary binding site (red tubes). (D, F, H) Depiction highlighting RMSF in one monomer of the protein, ligand-free protein in (D), M^{pro}-HL-3-68 complex in (F), and M^{pro}-**1** complex in (H). (E) Putty representation of the RMSF of the M^{pro} dimer complexed with HL-3-68. (G) Putty representations of the RMSF of the M^{pro} dimer complexed with compound **1**. The ligands in each case are highlighted using a ball-and-stick representation.

HL-3-68 and M^{pro}-Mcule-CSR-494190-S1 complexes (Figure 3c). In both structures, the Met49 side chain is sterically rotated away from its position in M^{pro}-**1** to accommodate the additional Cl atom, which enables van der Waals contacts with Cys44 but does not lead to an additional shift in the position of the S2 helix.

Crystal structures of complexes exhibiting similar or worse potency compared to compound **1** were also analyzed to assess the structural determinants of noncovalent ligand binding to M^{pro}. HL-3-78 substitutes Br at the P2 4-position probing the effect of a slightly larger van der Waals radius at this position compared to compound **1**. The binding of HL-3-78 resulted in no significant changes in the protein structure but comparable inhibition properties. However, bulkier and highly electronegative CF_3 groups at the 3- or 4-position (HL-3-52/63) bring about unfavorable distal shifts in the flexible S5 loop (>1.5 Å for Ala191 Cα, Figure S5a). Tyr54's phenol oxygen faces the S2 subsite and presents an attractive target for direct H-bonding, as tested by substituting CH_2OH (HL-3-71) and CHO (HL-3-70) at the 4-position of the P2. Unfortunately, the M^{pro}-HL-3-70 and M^{pro}-HL-3-71 crystal structures show the primary alcohol and the aldehyde oxygens are rotated away from the Tyr54 phenol oxygen, which keeps its conserved hydrogen bond with the main chain carbonyl of Asp187 (Figure S5b). Eliminating the cationic potential of the ligand by changing the linker from piperazine to piperidine (HL-3-69) produced no significant structural changes, except for a 0.4 Å shift in the position of the linker and P2 groups away from the S2 helix reducing van der Waals contacts.

Molecular Dynamics (MD) Simulations. MD simulations of M^{pro} (ligand-free), the M^{pro}-HL-3-68, and M^{pro}-**1** complexes reveal a consistent picture of how the HL-3-68 ligand is more stable within the primary binding site of M^{pro} compared to compound **1** reported in our previous study.[40] We quantified the conformational changes using the root-mean-square deviation (RMSD) analysis across each trajectory

https://doi.org/10.1021/acs.jmedchem.1c01475
J. Med. Chem. XXXX, XXX, XXX−XXX

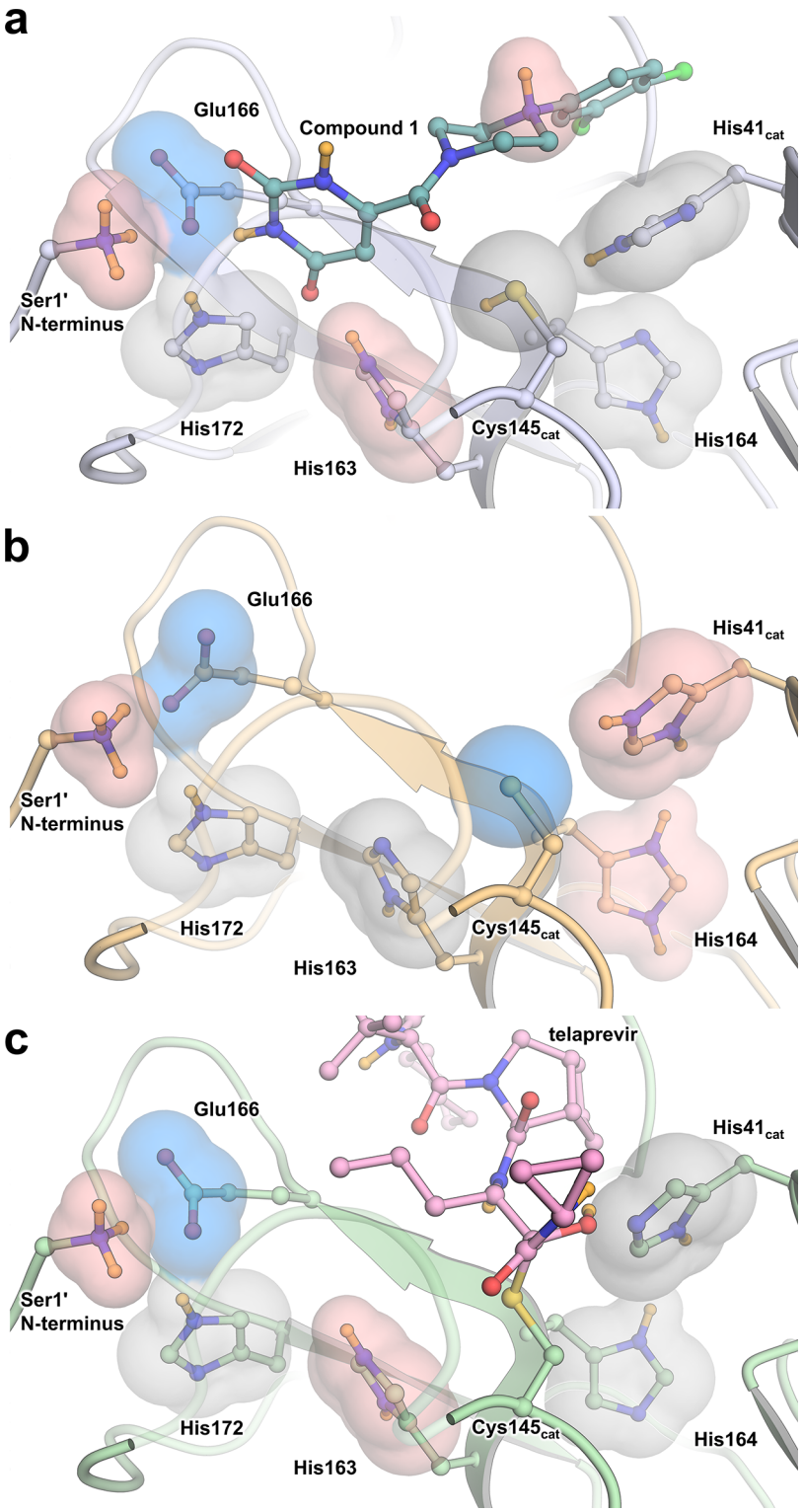

Figure 5. Comparison of protonation states of ionizable residues in the active site of SARS-CoV-2 M^{pro} determined from neutron crystallographic structures. (a) M^{pro} bound to compound **1**. (b) Ligand-free M^{pro} (PDB code 7JUN). (c) M^{pro} complexed with covalent α-ketoamide HCV protease inhibitor telaprevir (PDB code 7LB7). Charges are represented with transparent surface colored gray for neutral, red for positively charged, and blue for negatively charged. Nonpolar deuterium atoms are shown in orange. M^{pro}-**1** determined at pD = 7.4 and 7JUN and 7LB7 are at pH = 7.0.

(Figures 4 and S6). The distribution of the RMSDs determined from at least three replicates of the simulations (shown in Figure 4A as a histogram of all conformers from MD trajectories) further reveals that HL-3-68 stabilizes the binding pocket of M^{pro} more than compound **1**. For each system, we did observe slightly different fluctuations in chain A and chain B, which agrees with the previous simulation results.[13,40] Across the three simulation systems, the M^{pro}-HL-3-68 complex had the lowest average RMSD from both chains when compared with M^{pro} and the M^{pro}-**1** system (Figure S6).

https://doi.org/10.1021/acs.jmedchem.1c01475
J. Med. Chem. XXXX, XXX, XXX−XXX

Table 3. Summary of Protonation States and Corresponding Electric Charges of the Ionizable Residues in the SARS-CoV-2 M^{pro} Active Site Observed in the Neutron Structures of the Ligand-Free Enzyme and in Complex with Compound 1 and Telaprevir

	M^{pro} ligand-free (PDB ID 7JUN)		M^{pro}-Telaprevir (PDB ID 7LB7)		M^{pro}-1 (PDB ID 7N8C)	
residue	charge	species	charge	species	charge	species
$Cys145_{cat}$	−1	thiolate ($-S^-$)	0	S-C-OD (hemithioketal)	0	thiol (−SD)
$His41_{cat}$	+1	Nδ1-D, Nε2-D	0	Nδ1-D	0	Nε2-D
His163	0	Nδ1-D	+1	Nδ1-D, Nε2-D	+1	Nδ1-D, Nε2-D
His164	+1	Nδ1-D, Nε2-D	0	Nδ1-D	0	Nε2-D
His172	0	Nε2-D	0	Nε2-D	0	Nε2-D
net charge	+1		+1		+1	

Per-residue fluctuations were characterized by calculating the root-mean-square fluctuations (RMSF) of the Cα-atoms using the average conformation of each trajectory as the reference structure. Despite the fluctuation at the C-termini, the fluctuation patterns are largely in agreement, except that the M^{pro}-HL-3-68 system depicts suppressed fluctuations across the entire protein (Figure 4). Lower RMSFs were observed for the primary ligand-binding site of the M^{pro}-HL-3-68 system, whereas other regions remained largely unaffected by the binding of the ligand(s). In our previous simulations[40] and as demonstrated here, compound **1** can potentially move away from the primary binding site to occupy various novel sites on the surface of M^{pro}; however, in crystallographic studies, compound **1** has not been observed to bind to other sites. Given that both crystallographic studies and biochemical assays indicate that the HL-3-68 is more stabilizing, our simulations also confirm that over the course of the time-scales of our simulations, it appears that the HL-3-68 stabilizes the primary interactions in S1 and S2 subsites by "locking" in the site, thus considerably reducing the flexibility of the loops surrounding the primary binding site. Thus, our analyses support the observation that HL-3-68 ligand binding stabilizes the M^{pro} structure, forming stronger interactions than compound **1**.

DISCUSSION

The design and development of small-molecule therapeutics are crucial components of the ongoing efforts to battle COVID-19 and to prepare for future pandemics.[43] SARS-CoV-2 M^{pro} is an attractive target for specific protease inhibitors that can be further developed into clinical drugs. Studying the structure, function, and inhibition of the enzyme in detail is important for accelerating this process. Similarly, understanding the SAR profile of the designed compounds is crucial to determine how structural, electronic, and electrostatic properties of certain chemical groups affect inhibitor binding to the M^{pro} active site. Therefore, our SAR study was guided by the XN structure of the M^{pro}-**1** complex, where hydrogen atom positions, protonation states, and electric charges of M^{pro} residues and compound **1** were directly determined, providing the most detailed information to date for an M^{pro} in complex with a noncovalent inhibitor.

We observed in the XN structure of M^{pro}-**1** that M^{pro} adapts protonation states of the active site residues to maintain a net +1 charge within the binding site found in ligand-free[41] and telaprevir-bound[42] M^{pro} (Figure 5 and Table 3). Protonation state modulations occur through His163 in the S1 subsite, Cys145, and the His41−D_2O_{cat}−His164 network. As predicted computationally,[44] His163's Nδ1 becomes protonated upon ligand binding. The active site electrostatics can thus be tuned to allow the Cys145 side chain to exist as a thiol in M^{pro}-**1** or as a thiolate primed for catalysis as observed in the ligand-free form. The imidazole ring of His41 is not only flipped 180° relative to its conformation in the ligand-free and telaprevir complexes but also neutral. Hence, while the catalytic dyad is zwitterionic in the ligand-free structure, it is neutral in M^{pro}-**1**. Whether the protonation states of the Cys−His dyad are interdependent is currently an open question. Each protonation state combination of His41 and His164 has now been captured individually in the three neutron structures, suggesting that D_2O_{cat}-mediated H-bonding between these two side chains is not required for inhibition or a stable active site. Taken together, the protonation states determined from these three neutron structures suggest a mechanism where charges are shuffled between His163, the catalytic dyad, and His164 maintaining an overall +1 charge by active site residues when binding to inhibitors.

The hydrogen bond between the P1 group of the HL-3 compounds and the protonated positively charged His163 is essential for binding. Distorting the P1 group planarity by introducing a partial saturation as in compounds HL-3-51/53 appears to disrupt the hydrogen bond leading to a dramatic loss of affinity. The cationic nature of the linker positioned above the neutral catalytic dyad is beneficial for the compound's potency. However, the antiviral activity of some cationic drugs may be attributed to induced phospholipidosis rather than their specific function;[45] thus, novel M^{pro} inhibitors should be designed with this knowledge in mind. We determined that the substituents on the aromatic P2 group should have both moderate steric size and electronegativity as the binding is sensitive to small changes in atomic properties. In addition, compounds with only one substituent on the P2 group are poor inhibitors. Highly electronegative substituents such as F or CF_3 are disadvantageous, as are less electronegative but sterically larger CHO and CH_2OH, which push against the S5 loop and Tyr54, respectively. Adding a third Cl to position 5 of the P2 group in compound **1** to give HL-3-68 improved inhibition by 2−3-fold based on K_i and K_d values, indicating that its proximity to Cys44 and 3.5−4.3 Å contacts is favorable.

It is interesting that our ITC measurements of compound **1**, Mcule-CSR-494190-S1, and HL-3-68 binding to M^{pro} demonstrated that these noncovalent inhibitors bind with a limited hydrophobic effect, *i.e.*, the entropy (ΔS) of binding is small. A combination of several opposing factors may result in the measured values of ΔS of binding. First, the ligand-free M^{pro} has a few water molecules in the active site,[41] whereas several waters are recruited from the bulk solvent when the inhibitors bind. Second, the P2 groups access the S2 subsite by carving out the pocket blocked by Met49 and the S2 helix, limiting the

https://doi.org/10.1021/acs.jmedchem.1c01475
J. Med. Chem. XXXX, XXX, XXX−XXX

conformational space for favorable binding. Third, a compound would lose some conformational freedom once bound to M^{pro}. These three factors would contribute unfavorably to the ΔS of binding, while the loss of the compound's hydration shell when it binds to the enzyme would increase the entropy, contributing favorably to the ΔS of binding. In this way, substituting Cl with CH_3 at the 4-position of the P2 produces enough difference in conformational entropy and hydration entropy to elicit significant differences in the ΔS of binding. Changes in the protein dynamics upon inhibitor binding, and specifically, in the vibrational dynamics,[46−48] would also contribute to the ΔS (and ΔH) of binding, although the effect of these changes is not known.

CONCLUSIONS

In summary, the current SAR study of M^{pro} combines neutron and X-ray crystallography, chemical synthesis, *in vitro* measurements, and molecular dynamics simulations to profile the binding of a noncovalent ligand discovered through a new high-throughput screening approach.[40] Protonation states of critical side chains in the M^{pro} active site are intrinsically variable, thus hard to predict, a feature that presents challenges for *in silico* modeling and inhibitor design. The active site and especially the hydrophobic S2 pocket are sensitive to small changes in ligand properties. We show that one atom differences in the studied noncovalent ligand's P2 group were enough to significantly alter the binding entropy, potency, and complex dynamics. Taken together, these characterization techniques elucidate new details of M^{pro} as a drug target.

EXPERIMENTAL SECTION

General Information. Virtual reality-assisted analysis and model building were used to design and visualize derivatives of compound **1** (Mcule-5948770040). Modifications to the ligand scaffold starting from PDB code 7LTJ[40] were modeled and assessed using the MedChem tool in Nanome.[49,50] Nickel-nitrilotriacetic acid (Ni-NTA) columns were purchased from Cytiva (Piscataway, New Jersey). His-tagged human rhinovirus (HRV) 3C protease was purchased from Sigma (MilliporeSigma, St. Louis, MO). Crystallization reagents and supplies were purchased from Hampton Research (Aliso Viejo, California). Crystallographic supplies for crystal mounting and X-ray and neutron diffraction data collection at room temperature were purchased from MiTeGen (Ithaca, New York) and Vitrocom (Mountain Lakes, New Jersey). The FRET substrate DABCYL-KTSAVLQSGFRKM-E(EDANS) trifluoroacetate salt was purchased from Bachem (PN 4045664). NMR spectra were obtained on a Bruker Avance NEO NMR console coupled to an 11.74 T actively shielded magnet (Magnex Scientific/Varian) operating at 499.717 MHz for proton at the Center for Nanophase Materials Sciences. Mcule-5948770040 and 3,5-dichloro,4-methylphenyl derivative (Mcule-CSR-494190-S1) were purchased from Mcule, Inc (Palo Alto, California). All HL-3 compounds were synthesized at the Center for Nanophase Materials Sciences (Oak Ridge National Laboratory). Full details of the syntheses, NMR, and laser desorption ionization-time of flight (LDI-TOF) structural data are provided in the Supporting Information section.

General Synthesis Procedure of HL-3 Compounds.

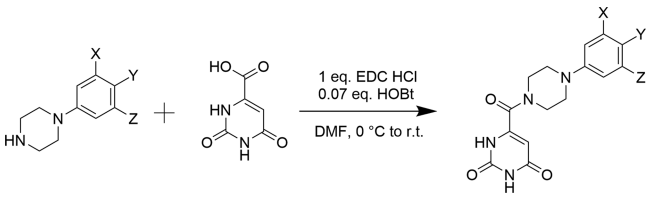

The HL-3 compounds were synthesized using techniques described previously.[51] In a typical procedure, a 20 mL vial was charged with a stir bar, the appropriate aryl piperazine derivative (1 equiv), orotic acid (1 equiv), HOBt·H_2O (0.07 equiv), and anhydrous dimethylformamide (DMF) (5 mL) at ambient temperature. The solution was cooled to 0 °C, and *N*-(3-dimethylaminopropyl)-*N*′-ethylcarbodiimide hydrochloride (EDC·HCl) (1 equiv) was added. The reaction mixture was stirred at room temperature overnight, and DMF was removed under reduced pressure. The residue was purified by silica gel chromatography (DCM to DCM/CH_3OH = 10:1). The removal of the solvents yielded the products as solids in yields >90%. Purity is >95% for all compounds as measured by NMR and mass spectrometry analyses (see the Supporting Information).

Gene Construction, Expression, and Purification of Hydrogenated and Partially Deuterated SARS-CoV-2 M^{pro}. A codon-optimized gene sequence of M^{pro} (NSP5) from SARS-CoV-2 was cloned into a plasmid harboring the kanamycin resistance cassette (pD451-SR, Atum, Newark, CA). The M^{pro} construct is flanked upstream by a gene for maltose-binding protein (MBP) and downstream by a His_6 tag.[52] The native N-terminus is achieved during expression through an M^{pro} autoprocessing site SAVLQ↓SGFRK, where ↓ denotes the cleavage site, corresponding to the cleavage between NSP4 and NSP5 in the viral polyprotein. The native C-terminus is produced through an HRV-3C protease cleavage site (SGVTFQ↓GP). This strategy enables a two-step Ni-affinity chromatography purification. Hydrogenated M^{pro} was expressed in *Escherichia coli* and purified according to the established procedures.[52] Partially deuterated M^{pro} was expressed using a bioreactor and purified, as described recently.[42] Final protein yields for hydrogenated M^{pro} preparations averaged ∼4 mg per 1 g cells (∼17 mg/L of cell culture), whereas partially deuterated preparations yielded ∼0.8 mg per 1 g of cell paste (∼40 mg/L of cell culture).

Similar in strategy to the above, a second construct was also used to express and purify the wild-type M^{pro}. This construct differs from the first construct by having an additional 36 residue spacer sequence corresponding to the immunoglobulin-binding domain B1 of GB1 inserted between MBP and a 6-amino-acid flanking nsp4 sequence TSAVLQ. Expression and purification were carried out, as described above and in ref 39. Peak fractions were concentrated and stored in aliquots at −20 °C. This second source of M^{pro} was used to determine the binding constants by ITC independent of the measurement carried out through enzyme kinetic measurements using the first enzyme source.

Crystallization of the M^{pro}−Inhibitor Complexes. Detailed instructions for crystallizing high-quality M^{pro} crystals starting from hydrogenated and partially deuterated enzymes are accessible.[42,53] Crystallization conditions for flower-shaped crystal aggregates of M^{pro} were initially discovered by automated high-throughput screening at the Hauptman-Woodward Medical Research Institute (HWI).[54] Crystal aggregates of apo-M^{pro} were reproduced locally and converted into microseeds for seeding subsequent crystallization experiments. Protein for co-crystallization was concentrated to 5 mg/mL in 20 mM Tris, 150 mM NaCl, and 1 mM tris(2-carboxyethyl)phosphine (TCEP), pH 8.0, and used fresh or stored at −30 °C for no longer than 2 weeks. Stock derivatives (50 mM) of compound **1** were prepared in 100% dimethyl sulfoxide (DMSO) for crystallization purposes and stored at −30 °C. M^{pro} was mixed with the ligands at a 1:5 molar ratio and allowed to incubate at room temperature for a minimum of 30 min prior to setting up crystal trays. All crystals grown for room-temperature X-ray diffraction used sitting drop vapor diffusion methodology with 18−21% poly(ethylene glycol) 3350 (PEG3350), 0.1 M Bis−Tris, pH 6.5 or 7.0, as the precipitant solution. Crystallization drop volumes of 20−30 μL at a 1:1 ratio were seeded with 0.2 μL of apo-M^{pro} microseeds (1:200 dilution). Crystals appeared after 3 days of incubation at 14 °C and continued to grow in volume for additional 7 days. Typical M^{pro}−ligand complex crystals grew to ∼0.1 mm^3 before mounting in MiTeGen (Ithaca, NY) room-temperature capillary setups (Figure S7).

The crystal used for joint XN crystallography started from partially deuterated M^{pro} at 10 mg/mL mixed with compound **1** at a 1:5 molar

https://doi.org/10.1021/acs.jmedchem.1c01475
J. Med. Chem. XXXX, XXX, XXX−XXX

ratio, incubated at room temperature for 30 min, and filtered through the 0.2 μm centrifugal filter. A Hampton nine-well sandwich box was set up with 220 μL of drops at a 1:1 ratio of protein to 18% PEG3350, 0.1 M Bis−Tris, pH 7.0, reservoir solution and 0.2 μL of microseeds at 1:200 dilution. After 11 days of incubation at 14 °C, the temperature was reduced to 12 °C, and crystals were allowed to grow for 30 more days. This process afforded three protein crystals of >2 mm^3 in volume, with the final crystal used for neutron data collection measuring ~2 × 1.5 × 0.7 mm^3 (2.1 mm^3) (Figure S8). The crystal was mounted in a fused quartz capillary accompanied by 19% PEG3350 prepared with 100% D_2O to allow labile hydrogens to exchange at 18 °C for 2 weeks before starting neutron data collection. The final pH of the crystallization drop at the time of crystal mounting was 7.0 as measured by a microelectrode, corresponding to a final pD of 7.4 (pD = pH + 0.4).

Room-Temperature X-ray Diffraction Data Collection and Structure Refinement. All room-temperature X-ray crystallographic data were collected with a Rigaku HighFlux HomeLab instrument equipped with a MicroMax-007 HF X-ray generator, Osmic VariMax optics, and a DECTRIS Eiger R 4M hybrid photon counting detector. Diffraction data were integrated using the CrysAlis Pro software suite (Rigaku Inc., The Woodlands, TX) and then reduced and scaled using Aimless[55] from the CCP4 suite.[56] Structures were solved by molecular replacement using PDB code 7LTJ[40] with Phaser[57] from CCP4. Each model was iteratively refined using Phenix.refine from PHENIX suite[58] and COOT[59,60] graphics program aided by Molprobity[61] for geometry validation. All ligand restraints were generated with eLBOW[62] using geometry optimized by quantum mechanical calculations in Gaussian 16 at the B3LYP/6-31g(d,p) level of theory.[63] Final data collection and refinement statistics are organized in Table S2.

Neutron Diffraction Data Collection. Room-temperature neutron diffraction data were collected using the Macromolecular Neutron Diffractometer Instrument (MaNDi) at the Spallation Neutron Source of the Oak Ridge National Laboratory.[64−66] The crystal was held stationary at room temperature, while diffraction data were collected for 20 h using all neutrons between 2 and 4.16 Å. Following this, the crystal was rotated by $\Delta\phi = 10°$, and a subsequent data frame was collected again for 20 h. A total of 21 data frames were collected in the final neutron data set. Diffraction data were reduced using the Mantid package, with integration carried out using three-dimensional TOF profile fitting.[67] Wavelength normalization of the Laue data was performed using the Lauenorm program from the Lauegen suite.[68] Neutron data collection statistics are shown in Table S1.

Joint X-ray/Neutron (XN) Refinement. Joint XN refinement of the deuterated M^{pro}-**1** complex was performed using nCNS,[69,70] and the structure was manipulated in COOT.[59,60] After initial rigid-body refinement, several cycles of positional, atomic displacement parameter, and occupancy refinement were run. Correctness of side-chain conformations, hydrogen bonding, and orientations of D_2O water molecules in the structure was based on the $mF_o - DF_c$ difference neutron scattering length density maps. The $mF_o - DF_c$ and $mF_o - DF_c$ neutron scattering length density maps were then examined to determine the correct orientations of hydroxyl (Ser, Thr, Tyr), thiol (Cys), and ammonium (Lys) groups as well as protonation states of the enzyme residues and compound **1**. The protonation states of some disordered side chains on the protein surface could not be obtained directly and remained ambiguous. Water molecules were refined as D_2O where water oxygen atoms were centered on their electron density peaks and each molecule was rotated in accordance with the neutron scattering length density maps. Hydrogen positions in the protein were modeled as deuterium atoms because the protein was partially deuterated. Compound **1** is ionizable at the piperazine amine and was modeled as the protonated species with a D atom. Occupancies of D atoms were refined individually within the range of −0.56 (pure H) to 1.00 (pure D) because the neutron scattering length of H is −0.56 times that of D. Before depositing the neutron structure to the PDB, coordinates of a D atom were split into two records corresponding to an H and a D partially occupying the same site, both with positive partial occupancies that add up to unity. The percent D at a specific site is calculated according to the following formula: % D = {occupancy(D) + 0.56}/1.56.

Enzyme Inhibition Assay. Compounds were dissolved in 10 mM DMSO and stored at −20 °C. The initial rates of M^{pro} were measured, and the data were analyzed using a previously established fluorescence resonance energy transfer (FRET) peptide substrate assay method.[71,72] For the initial inhibition screen, performed in duplicate, final assay concentrations were 250 nM enzyme, 20 μM inhibitor, and 40 μM peptide substrate. Inhibitors with 50% residual activity or less in the initial screen were further characterized across seven inhibitor concentrations in the range of 0.03−100 μM in at least duplicate, and the resulting initial rates were normalized with 0 as 0% residual activity and the average of positive control rates without the inhibitor as 100% residual activity. The [inhibitor] *vs* normalized response−variable slope equation in GraphPad Prism 9 was fit to the normalized data to determine IC_{50} values

$$A = \frac{100}{1 + \left(\frac{IC_{50}}{[I]}\right)^{b}} \quad (1)$$

where A is the residual activity, IC_{50} is the inhibitor concentration at which 50% inhibition is observed, [I] is the inhibitor concentration, and b is the Hill slope.

The two inhibitors with the lowest IC_{50} values were further characterized to determine their K_i values, as previously described for compound **1**.[40] Initial rates were measured in triplicate without the inhibitor and with the inhibitor at final concentrations of 2.5, 7.5, and 25 μM, with 150 nM enzyme, and final concentrations of the substrate in the range 20−500 μM. The competitive inhibition equation in GraphPad Prism 9 was fit to the resulting initial rates, v_0, to determine the Michaelis−Menten enzyme parameters V_{max} and K_M and the K_i affinities of the inhibitors.

$$v_0 = \frac{V_{max}[S]}{K_M\left(1 + \frac{[I]}{K_i}\right) + [S]} \quad (2)$$

Isothermal Titration Calorimetry. Purified wild-type M^{pro} was diluted from a stock solution to 60 μM and dialyzed overnight at 4 °C against 25 mM Tris−HCl, pH 7.2, 20 mM NaCl, and 1 mM TCEP (ITC buffer). The concentration of the enzyme was estimated based on its 280 nm absorbance. Stock solutions of inhibitors were diluted in ITC buffer to 0.3 mM and contained a final concentration of 0.5% DMSO. The protein solution was also adjusted to contain the same concentration of DMSO. Titrations were performed at 28 °C on an iTC200 microcalorimeter (Malvern Instruments Inc., Westborough, Massachusetts). A control titration of buffer with the inhibitor showed a negligible response. Data were processed and plots were generated using the Origin software provided with the instrument. For competitive inhibitors that bind at only one site, the dissociation constant ($K_d = 1/K_a$) is equivalent to the inhibition constant measured by enzyme kinetics (K_i).

MD Simulations and Analysis. MD simulations were performed for three different systems (ligand-free, or apo-, M^{pro}; M^{pro} in complex with compound **1**; and M^{pro} with HL-3-68) to study the protein stability upon binding with different ligands. The simulation runs were carried out with the OpenMM package on Nvidia V100 GPUs. The protein atomic interactions were described with the Amberff14SB force field and tip3p water model. The ligands, compound **1**, and HL-3-68 were modeled using the antechamber package with the GAFF force field. Each system was neutralized with counterions. The nonbonded interactions were cut off at 10 Å and long-range interactions were calculated with the particle mesh Ewald method. The simulations were run at 310 K and 2 fs time steps with the Langevin integrator. The chemical bonds with hydrogen atoms were fixed, and the system pressure was fixed at 1 bar with a Monte Carlo barostat. Each of the three systems was equilibrated using a procedure described in the previous work[40] and three replicas (each with a 250 ns production run) were generated; snapshots from the simulation

https://doi.org/10.1021/acs.jmedchem.1c01475
J. Med. Chem. XXXX, XXX, XXX−XXX

were saved every 50 ps. For all of the trajectories, we calculated the root-mean-square deviations (RMSDs) for the overall protein structure and root-mean-square fluctuation (RMSF) to quantify per-residue fluctuations.

Antiviral Assays. Evaluation of the antiviral activity of compound **1** (Mcule-59487700), HL-3-68, and Mcule-CSR-494190-S1 was carried out in Vero E6 TMPRSSS cells, as described in Bocci et al.[73] using the USA-WA1/2020 (deposited by the Centers for Disease Control and Prevention and obtained through BEI Resources, NIAID, NIH, NR-52281). Compounds were evaluated in a dose response format starting at 33 μM and 6 additional twofold dilutions in duplicate. These compounds demonstrated no antiviral activity.

■ ASSOCIATED CONTENT

Supporting Information

The Supporting Information is available free of charge at https://pubs.acs.org/doi/10.1021/acs.jmedchem.1c01475.

Crystallographic data collection and refinement statistics for the joint X-ray/neutron structure of SARS-CoV-2 M^{pro} in complex with compound **1** (Table S1); data reduction and refinement statistics for the room temperature X-ray crystal structures of SARS-CoV-2 M^{pro}-inhibitor complexes used in this study (Table S2); superpositions of M^{pro}-**1** with M^{pro} ligand-free and M^{pro}-telaprevir neutron structures (Figure S1); cytotoxicity and antiviral activity of the selected molecules against SARS-CoV-2 (Figure S2); binding isotherms for the interaction of compound **1** and its analogues with M^{pro} (Figure S3); electron density for ligands from room temperature X-ray co-crystal structures (Figure S4); superpositions of M^{pro}-**1** X-ray/neutron structure with selected HL-3 complex structures (Figure S5); RMSD of MD simulation trajectories (Figure S6); crystals of M^{pro}-inhibitor complexes used (Figure S7); pre-mounted crystal of ~2.1 mm^3 dM^{pro}-**1** complex used for neutron diffraction and subsequent X-ray data collection (Figure S8); materials and methods, ^1H and ^{13}C NMR spectra, and mass spectra (PDF)

Molecular formula strings (CSV)

■ AUTHOR INFORMATION

Corresponding Authors

Peter V. Bonnesen − *National Virtual Biotechnology Laboratory, US Department of Energy, Washington, District of Columbia 20585, United States; Center for Nanophase Materials Sciences, Oak Ridge National Laboratory, Oak Ridge, Tennessee 37831, United States;* Email: bonnesenpv@ornl.gov

Andrey Kovalevsky − *Neutron Scattering Division, Oak Ridge National Laboratory, Oak Ridge, Tennessee 37831, United States; National Virtual Biotechnology Laboratory, US Department of Energy, Washington, District of Columbia 20585, United States;* orcid.org/0000-0003-4459-9142; Email: kovalevskyay@ornl.gov

Authors

Daniel W. Kneller − *Neutron Scattering Division, Oak Ridge National Laboratory, Oak Ridge, Tennessee 37831, United States; National Virtual Biotechnology Laboratory, US Department of Energy, Washington, District of Columbia 20585, United States;* orcid.org/0000-0002-5416-5789

Hui Li − *National Virtual Biotechnology Laboratory, US Department of Energy, Washington, District of Columbia 20585, United States; Center for Nanophase Materials Sciences, Oak Ridge National Laboratory, Oak Ridge, Tennessee 37831, United States;* orcid.org/0000-0002-6964-9962

Stephanie Galanie − *National Virtual Biotechnology Laboratory, US Department of Energy, Washington, District of Columbia 20585, United States; Biosciences Division, Oak Ridge National Laboratory, Oak Ridge, Tennessee 37831, United States*

Gwyndalyn Phillips − *Neutron Scattering Division, Oak Ridge National Laboratory, Oak Ridge, Tennessee 37831, United States; National Virtual Biotechnology Laboratory, US Department of Energy, Washington, District of Columbia 20585, United States*

Audrey Labbé − *National Virtual Biotechnology Laboratory, US Department of Energy, Washington, District of Columbia 20585, United States; Biosciences Division, Oak Ridge National Laboratory, Oak Ridge, Tennessee 37831, United States*

Kevin L. Weiss − *Neutron Scattering Division, Oak Ridge National Laboratory, Oak Ridge, Tennessee 37831, United States; National Virtual Biotechnology Laboratory, US Department of Energy, Washington, District of Columbia 20585, United States;* orcid.org/0000-0002-6486-8007

Qiu Zhang − *Neutron Scattering Division, Oak Ridge National Laboratory, Oak Ridge, Tennessee 37831, United States; National Virtual Biotechnology Laboratory, US Department of Energy, Washington, District of Columbia 20585, United States*

Mark A. Arnould − *National Virtual Biotechnology Laboratory, US Department of Energy, Washington, District of Columbia 20585, United States; Center for Nanophase Materials Sciences, Oak Ridge National Laboratory, Oak Ridge, Tennessee 37831, United States*

Austin Clyde − *National Virtual Biotechnology Laboratory, US Department of Energy, Washington, District of Columbia 20585, United States; Data Science and Learning Division, Argonne National Laboratory, Lemont, Illinois 60439, United States; Department of Computer Science, University of Chicago, Chicago, Illinois 60615, United States*

Heng Ma − *National Virtual Biotechnology Laboratory, US Department of Energy, Washington, District of Columbia 20585, United States; Data Science and Learning Division, Argonne National Laboratory, Lemont, Illinois 60439, United States*

Arvind Ramanathan − *National Virtual Biotechnology Laboratory, US Department of Energy, Washington, District of Columbia 20585, United States; Data Science and Learning Division, Argonne National Laboratory, Lemont, Illinois 60439, United States; Consortium for Advanced Science and Engineering, University of Chicago, Chicago, Illinois 60615, United States;* orcid.org/0000-0002-1622-5488

Colleen B. Jonsson − *Department of Microbiology, Immunology and Biochemistry, University of Tennessee Health Science Center, Memphis, Tennessee 38163, United States;* orcid.org/0000-0002-2640-7672

Martha S. Head − *National Virtual Biotechnology Laboratory, US Department of Energy, Washington, District of Columbia 20585, United States; Joint Institute for Biological Sciences, Oak Ridge National Laboratory, Oak Ridge, Tennessee 37831, United States*

Leighton Coates − *National Virtual Biotechnology Laboratory, US Department of Energy, Washington, District*

of Columbia 20585, United States; Second Target Station, Oak Ridge National Laboratory, Oak Ridge, Tennessee 37831, United States; orcid.org/0000-0003-2342-049X

John M. Louis − *Laboratory of Chemical Physics, National Institute of Diabetes and Digestive and Kidney Diseases, National Institutes of Health, DHHS, Bethesda, Maryland 20892-0520, United States*

Complete contact information is available at: https://pubs.acs.org/10.1021/acs.jmedchem.1c01475

Author Contributions

D.W.K., L.C, M.S.H., P.V.B., and A.K. designed the study. G.P. and Q.Z. expressed the protein. D.W.K. purified the protein. K.L.W. and Q.Z. performed protein deuteration. D.W.K. and A.K. crystallized the protein and inhibitor complexes. D.W.K., L.C., and A.K. collected X-ray and neutron data, reduced the data, and refined the structures. H.L. and P.V.B. synthesized compounds. S.G. and A.L. performed *in vitro* inhibition assays. J.M.L. produced a second source of M^{pro} and performed ITC experiments. M.A.A. collected mass spectrometry data. C.B.J. performed antiviral assays. D.W.K., H.L., P.V.B., S.G., and A.K. wrote the paper with help from all co-authors.

Notes

The authors declare no competing financial interest.

The coordinates and structure factors for the joint X-ray/neutron structure of the SARS-CoV-2 M^{pro}-Compound **1** complex have been deposited in the PDB with the accession code 7N8C. The coordinates and structure factors for the room-temperature X-ray structures of other reported complexes have been deposited in the PDB with the accession codes as follows: 7RLS for M^{pro}-HL-3-68, 7RM2 for M^{pro}-Mcule-CSR-494190-S1, 7RMB for M^{pro}-HL-3-78, 7RME for M^{pro}-HL-3-52, 7RMT for M^{pro}-HL-3-70, 7RMZ for M^{pro}-HL-3-63, 7RN4 for M^{pro}-HL-3-69, 7RNH for M^{pro}-HL-3-45, and 7RNK for M^{pro}-HL-3-71. Authors will release the atomic coordinates upon article publication. Any other relevant data are available from the corresponding authors upon reasonable request.

■ ACKNOWLEDGMENTS

This research was supported by the DOE Office of Science through the National Virtual Biotechnology Laboratory (NVBL), a consortium of DOE national laboratories focused on the response to COVID-19, with funding provided by the Coronavirus CARES Act. This research used resources at the Center for Nanophase Materials Sciences, the Spallation Neutron Source, and the HighFlux Isotope Reactor, which are DOE Office of Science User Facilities operated by the Oak Ridge National Laboratory. The Office of Biological and Environmental Research supported research at ORNL's Center for Structural Molecular Biology (CSMB), a DOE Office of Science User Facility. This research used resources of the Spallation Neutron Source Second Target Station Project at the Oak Ridge National Laboratory (ORNL). ORNL is managed by UT-Battelle LLC for DOE's Office of Science, the single largest supporter of basic research in the physical sciences in the United States. The authors thank Dr. Hugh M. O'Neill from ORNL for assistance during expression of the partially deuterated protein. L.C. acknowledges support from the NIH (R01-GM071939). They also thank Annie Aniana from the National Institute of Diabetes and Digestive and Kidney Diseases (NIDDK) for excellent technical assistance. This work was also supported by the Intramural Research Program of NIDDK, NIH.

■ ABBREVIATIONS USED

SARS-CoV-2, severe acute respiratory syndrome coronavirus 2; 3CL M^{pro}, chymotrypsin-like main protease, M^{pro}, wild-type main protease of SARS-CoV-2

■ REFERENCES

(1) Gavor, E.; Choong, Y. K.; Er, S. Y.; Sivaraman, H.; Sivaraman, J. Structural Basis of SARS-CoV-2 and SARS-CoV Antibody Interactions. *Trends Immunol.* **2020**, *41*, 1006−1022.

(2) Meo, S. A.; Bukhari, I. A.; Akram, J.; Meo, A. S.; Klonoff, D. C. COVID-19 Vaccines: Comparison of Biological, Pharmacological Characteristics and Adverse Effects of Pfizer/BioNTech and Moderna Vaccines. *Eur. Rev. Med. Pharmacol. Sci.* **2021**, *25*, 1663−1679.

(3) Doroftei, B.; Ciobica, A.; Ilie, O.-D.; Maftei, R.; Ilea, C. Mini-Review Discussing the Reliability and Efficiency of COVID-19 Vaccines. *Diagnostics* **2021**, *11*, No. 579.

(4) Bidram, E.; Esmaeili, Y.; Amini, A.; Sartorius, R.; Tay, F. R.; Shariati, L.; Makvandi, P. Nanobased Platforms for Diagnosis and Treatment of COVID-19: From Benchtop to Bedside. *ACS Biomater. Sci. Eng.* **2021**, *7*, 2150−2176.

(5) Wang, P.; Nair, M. S.; Liu, L.; Iketani, S.; Luo, Y.; Guo, Y.; Wang, M.; Yu, J.; Zhang, B.; Kwong, P. D.; Graham, B. S.; Mascola, J. R.; Chang, J. Y.; Yin, M. T.; Sobieszczyk, M.; Kyratsous, C. A.; Shapiro, L.; Sheng, Z.; Huang, Y.; Ho, D. D. Antibody Resistance of SARS-CoV-2 Variants B.1.351 and B.1.1.7. *Nature* **2021**, *593*, 130−135.

(6) Vilcek, S. SARS-CoV-2: Zoonotic Origin of Pandemic Coronavirus. *Acta Virol.* **2020**, *64*, 281−287.

(7) Singh, D.; Yi, S. V. On the Origin and Evolution of SARS-CoV-2. *Exp. Mol. Med.* **2021**, *53*, 537−547.

(8) Ghosh, A. K.; Brindisi, M.; Shahabi, D.; Chapman, M. E.; Mesecar, A. D. Drug Development and Medicinal Chemistry Efforts toward SARS-Coronavirus and Covid-19 Therapeutics. *ChemMedChem* **2020**, *15*, 907−932.

(9) Tong, L. Viral Proteases. *Chem. Rev.* **2002**, *102*, 4609−4626.

(10) Liu, Y.; Liang, C.; Xin, L.; Ren, X.; Tian, L.; Ju, X.; Li, H.; Wang, Y.; Zhao, Q.; Liu, H.; Cao, W.; Xie, X.; Zhang, D.; Wang, Y.; Jian, Y. The Development of Coronavirus 3C-Like Protease (3CLpro) Inhibitors from 2010 to 2020. *Eur. J. Med. Chem.* **2020**, *206*, No. 112711.

(11) Jin, Z.; Du, X.; Xu, Y.; Deng, Y.; Liu, M.; Zhao, Y.; Zhang, B.; Li, X.; Zhang, L.; Peng, C.; Duan, Y.; Yu, J.; Wang, L.; Yang, K.; Liu, F.; Jiang, R.; Yang, X.; You, T.; Liu, X.; Yang, X.; Bai, F.; Liu, H.; Liu, X.; Guddat, L. W.; Xu, W.; Xiao, G.; Qin, C.; Shi, Z.; Jiang, H.; Rao, Z.; Yang, H. Structure of Mpro from SARS-CoV-2 and Discovery of Its Inhibitors. *Nature* **2020**, *582*, 289−293.

(12) Ton, A. T.; Gentile, F.; Hsing, M.; Ban, F.; Cherkasov, A. Rapid Identification of Potential Inhibitors of SARS-CoV-2 Main Protease by Deep Docking of 1.3 Billion Compounds. *Mol. Inf.* **2020**, *39*, No. 2000028.

(13) Suárez, D.; Díaz, N. SARS-CoV-2 Main Protease: A Molecular Dynamics Study. *J. Chem. Inf. Model.* **2020**, *60*, 5815−5831.

(14) Acharya, A.; Agarwal, R.; Baker, M. B.; Baudry, J.; Bhowmik, D.; Boehm, S.; Byler, K. G.; Chen, S. Y.; Coates, L.; Cooper, C. J.; Demerdash, O.; Daidone, I.; Eblen, J. D.; Ellingson, S.; Forli, S.; Glaser, J.; Gumbart, J. C.; Gunnels, J.; Hernandez, O.; Irle, S.; Kneller, D. W.; Kovalevsky, A.; Larkin, J.; Lawrence, T. J.; LeGrand, S.; Liu, S.-H.; Mitchell, J. C.; Park, G.; Parks, J. M.; Pavlova, A.; Petridis, L.; Poole, D.; Pouchard, L.; Ramanathan, A.; Rogers, D. M.; Santos-Martins, D.; Scheinberg, A.; Sedova, A.; Shen, Y.; Smith, J. C.; Smith, M. D.; Soto, C.; Tsaris, A.; Thavappiragasam, M.; Tillack, A. F.; Vermaas, J. V.; Vuong, V. Q.; Yin, J.; Yoo, S.; Zahran, M.; Zanetti-Polzi, L. Supercomputer-Based Ensemble Docking Drug Discovery Pipeline with Application to Covid-19. *J. Chem. Inf. Model.* **2020**, *60*, 5832−5852.

(15) Pathak, N.; Chen, Y. T.; Hsu, Y. C.; Hsu, N. Y.; Kuo, C. J.; Tsai, H. P.; Kang, J. J.; Huang, C. H.; Chang, S. Y.; Chang, Y. H.; Liang, P. H.; Yang, J. M. Uncovering Flexible Active Site Conformations of SARS-CoV-2 3CL Proteases through Protease Pharmacophore Clusters and COVID-19 Drug Repurposing. *ACS Nano* **2021**, *15*, 857−872.
(16) Wu, F.; Zhao, S.; Yu, B.; Chen, Y.-M.; Wang, W.; Song, Z.-G.; Hu, Y.; Tao, Z.-W.; Tian, J.-H.; Pei, Y.-Y.; Yuan, M.-L.; Zhang, Y.-L.; Dai, F.-H.; Liu, Y.; Wang, Q.-M.; Zheng, J.-J.; Xu, L.; Holmes, E. C.; Zhang, Y.-Z. A New Coronavirus Associated with Human Respiratory Disease in China. *Nature* **2020**, *579*, 265−269.
(17) Xu, J.; Zhao, S.; Teng, T.; Abdalla, A. E.; Zhu, W.; Xie, L.; Wang, Y.; Guo, X. Systematic Comparison of Two Animal-to-Human Transmitted Human Coronaviruses: SARS-CoV-2 and SARS-CoV. *Viruses* **2020**, *12*, No. 244.
(18) Ullrich, S.; Nitsche, C. The SARS-CoV-2 Main Protease as Drug Target. *Bioorg. Med. Chem. Lett.* **2020**, *30*, No. 127377.
(19) Yang, K. S.; Ma, X. R.; Ma, Y.; Alugubelli, Y. R.; Scott, D. A.; Vatansever, E. C.; Drelich, A. K.; Sankaran, B.; Geng, Z. Z.; Blankenship, L. R.; Ward, H. E.; Sheng, Y. J.; Hsu, J. C.; Kratch, K. C.; Zhao, B.; Hayatshahi, H. S.; Liu, J.; Li, P.; Fierke, C. A.; Tseng, C. K.; Xu, S.; Liu, W. R. A Quick Route to Multiple Highly Potent SARS-CoV-2 Main Protease Inhibitors. *ChemMedChem* **2021**, *16*, 942−948.
(20) Hattori, S.-i.; Higashi-Kuwata, N.; Hayashi, H.; Allu, S. R.; Raghavaiah, J.; Bulut, H.; Das, D.; Anson, B. J.; Lendy, E. K.; Takamatsu, Y.; Takamune, N.; Kishimoto, N.; Murayama, K.; Hasegawa, K.; Li, M.; Davis, D. A.; Kodama, E. N.; Yarchoan, R.; Wlodawer, A.; Misumi, S.; Mesecar, A. D.; Ghosh, A. K.; Mitsuya, H. A Small Molecule Compound with an Indole Moiety Inhibits the Main Protease of SARS-CoV-2 and Blocks Virus Replication. *Nat. Commun.* **2021**, *12*, No. 668.
(21) Bai, B.; Belovodskiy, A.; Hena, M.; Kandadai, A. S.; Joyce, M. A.; Saffran, H. A.; Shields, J. A.; Khan, M. B.; Arutyunova, E.; Lu, J.; Bajwa, S. K.; Hockman, D.; Fischer, C.; Lamer, T.; Vuong, W.; Belkum, M. J.; van Gu, Z.; Lin, F.; Du, Y.; Xu, J.; Rahim, M.; Young, H. S.; Vederas, J. C.; Tyrrell, D. L.; Lemieux, M. J.; Nieman, J. A. Peptidomimetic α-Acyloxymethylketone Warheads with Six-Membered Lactam P1 Glutamine Mimic: SARS-CoV-2 3CL Protease Inhibition, Coronavirus Antiviral Activity, and in Vitro Biological Stability. *J. Med. Chem.* **2021**, DOI: 10.1021/ACS.JMEDCHEM.1C00616.
(22) Pillaiyar, T.; Manickam, M.; Namasivayam, V.; Hayashi, Y.; Jung, S. H. An Overview of Severe Acute Respiratory Syndrome-Coronavirus (SARS-CoV) 3CL Protease Inhibitors: Peptidomimetics and Small Molecule Chemotherapy. *J. Med. Chem.* **2016**, *59*, 6595−6628.
(23) Pillaiyar, T.; Meenakshisundaram, S.; Manickam, M. Recent Discovery and Development of Inhibitors Targeting Coronaviruses. *Drug Discovery Today* **2020**, *25*, 668−688.
(24) Hoffman, R. L.; Kania, R. S.; Brothers, M. A.; Davies, J. F.; Ferre, R. A.; Gajiwala, K. S.; He, M.; Hogan, R. J.; Kozminski, K.; Li, L. Y.; Lockner, J. W.; Lou, J.; Marra, M. T.; Mitchell, L. J.; Murray, B. W.; Nieman, J. A.; Noell, S.; Planken, S. P.; Rowe, T.; Ryan, K.; Smith, G. J.; Solowiej, J. E.; Steppan, C. M.; Taggart, B. Discovery of Ketone-Based Covalent Inhibitors of Coronavirus 3CL Proteases for the Potential Therapeutic Treatment of COVID-19. *J. Med. Chem.* **2020**, *63*, 12725−12747.
(25) Konno, S.; Kobayashi, K.; Senda, M.; Funai, Y.; Seki, Y.; Tamai, I.; Schäkel, L.; Sakata, K.; Pillaiyar, T.; Taguchi, A.; Taniguchi, A.; Gütschow, M.; Müller, C. E.; Takeuchi, K.; Hirohama, M.; Kawaguchi, A.; Kojima, M.; Senda, T.; Shirasaka, Y.; Kamitani, W.; Hayashi, Y. 3CL Protease Inhibitors with an Electrophilic Arylketone Moiety as Anti-SARS-CoV-2 Agents. *J. Med. Chem.* **2021**, DOI: 10.1021/ACS.JMEDCHEM.1C00665.
(26) Fu, L.; Ye, F.; Feng, Y.; Yu, F.; Wang, Q.; Wu, Y.; Zhao, C.; Sun, H.; Huang, B.; Niu, P.; Song, H.; Shi, Y.; Li, X.; Tan, W.; Qi, J.; Gao, G. F. Both Boceprevir and GC376 Efficaciously Inhibit SARS-CoV-2 by Targeting Its Main Protease. *Nat. Commun.* **2020**, *11*, No. 4417.
(27) Ma, C.; Sacco, M. D.; Hurst, B.; Townsend, J. A.; Hu, Y.; Szeto, T.; Zhang, X.; Tarbet, B.; Marty, M. T.; Chen, Y.; Wang, J. Boceprevir, GC-376, and Calpain Inhibitors II, XII Inhibit SARS-CoV-2 Viral Replication by Targeting the Viral Main Protease. *Cell Res.* **2020**, *30*, 678−692.
(28) Xia, Z.; Sacco, M.; Hu, Y.; Ma, C.; Meng, X.; Zhang, F.; Szeto, T.; Xiang, Y.; Chen, Y.; Wang, J. Rational Design of Hybrid SARS-CoV-2 Main Protease Inhibitors Guided by the Superimposed Cocrystal Structures with the Peptidomimetic Inhibitors GC-376, Telaprevir, and Boceprevir. *ACS Pharmacol. Transl. Sci.* **2021**, *4*, 1408−1421.
(29) Ghahremanpour, M. M.; Tirado-Rives, J.; Deshmukh, M.; Ippolito, J. A.; Zhang, C. H.; Cabeza De Vaca, I.; Liosi, M. E.; Anderson, K. S.; Jorgensen, W. L. Identification of 14 Known Drugs as Inhibitors of the Main Protease of SARS-CoV-2. *ACS Med. Chem. Lett.* **2020**, *11*, 2526−2533.
(30) Li, Z.; Li, X.; Huang, Y. Y.; Wu, Y.; Liu, R.; Zhou, L.; Lin, Y.; Wu, D.; Zhang, L.; Liu, H.; Xu, X.; Yu, K.; Zhang, Y.; Cui, J.; Zhan, C. G.; Wang, X.; Luo, H.-B. Identify Potent SARS-CoV-2 Main Protease Inhibitors via Accelerated Free Energy Perturbation-Based Virtual Screening of Existing Drugs. *Proc. Natl. Acad. Sci. U.S.A.* **2020**, *117*, 27381−27387.
(31) Douangamath, A.; Fearon, D.; Gehrtz, P.; Krojer, T.; Lukacik, P.; Owen, C. D.; Resnick, E.; Strain-Damerell, C.; Aimon, A.; Ábrányi-Balogh, P.; Brandão-Neto, J.; Carbery, A.; Davison, G.; Dias, A.; Downes, T. D.; Dunnett, L.; Fairhead, M.; Firth, J. D.; Jones, S. P.; Keeley, A.; Keserü, G. M.; Klein, H. F.; Martin, M. P.; Noble, M. E. M.; O'Brien, P.; Powell, A.; Reddi, R. N.; Skyner, R.; Snee, M.; Waring, M. J.; Wild, C.; London, N.; von Delft, F.; Walsh, M. A. Crystallographic and Electrophilic Fragment Screening of the SARS-CoV-2 Main Protease. *Nat. Commun.* **2020**, *11*, No. 5047.
(32) Günther, S.; Reinke, P. Y. A.; Fernández-Garciá, Y.; Lieske, J.; Lane, T. J.; Ginn, H. M.; Koua, F. H. M.; Ehrt, C.; Ewert, W.; Oberthuer, D.; Yefanov, O.; Meier, S.; Lorenzen, K.; Krichel, B.; Kopicki, J. D.; Gelisio, L.; Brehm, W.; Dunkel, I.; Seychell, B.; Gieseler, H.; Norton-Baker, B.; Escudero-Pérez, B.; Domaracky, M.; Saouane, S.; Tolstikova, A.; White, T. A.; Hänle, A.; Groessler, M.; Fleckenstein, H.; Trost, F.; Galchenkova, M.; Gevorkov, Y.; Li, C.; Awel, S.; Peck, A.; Barthelmess, M.; Schlünzen, F.; Xavier, P. L.; Werner, N.; Andaleeb, H.; Ullah, N.; Falke, S.; Srinivasan, V.; Franca, B. A.; Schwinzer, M.; Brognaro, H.; Rogers, C.; Melo, D.; Zaitseva-Doyle, J. J.; Knoska, J.; Peña-Murillo, G. E.; Mashhour, A. R.; Hennicke, V.; Fischer, P.; Hakanpää, J.; Meyer, J.; Gribbon, P.; Ellinger, B.; Kuzikov, M.; Wolf, M.; Beccari, A. R.; Bourenkov, G.; Stetten, D. Von.; Pompidor, G.; Bento, I.; Panneerselvam, S.; Karpics, I.; Schneider, T. R.; Garcia-Alai, M. M.; Niebling, S.; Günther, C.; Schmidt, C.; Schubert, R.; Han, H.; Boger, J.; Monteiro, D. C. F.; Zhang, L.; Sun, X.; Pletzer-Zelgert, J.; Wollenhaupt, J.; Feiler, C. G.; Weiss, M. S.; Schulz, E. C.; Mehrabi, P.; Karnĭcar, K.; Usenik, A.; Loboda, J.; Tidow, H.; Chari, A.; Hilgenfeld, R.; Uetrech, C.; Cox, R.; Zaliani, A.; Beck, T.; Rarey, M.; Günther, S.; Turk, D.; Hinrichs, W.; Chapman, H. N.; Pearson, A. R.; Betzel, C.; Meents, A. X-ray Screening Identifies Active Site and Allosteric Inhibitors of SARS-CoV-2 Main Protease. *Science* **2021**, *372*, 642−646.
(33) Zhang, C. H.; Stone, E. A.; Deshmukh, M.; Ippolito, J. A.; Ghahremanpour, M. M.; Tirado-Rives, J.; Spasov, K. A.; Zhang, S.; Takeo, Y.; Kudalkar, S. N.; Liang, Z.; Isaacs, F.; Lindenbach, B.; Miller, S. J.; Anderson, K. S.; Jorgensen, W. L. Potent Noncovalent Inhibitors of the Main Protease of SARS-CoV-2 from Molecular Sculpting of the Drug Perampanel Guided by Free Energy Perturbation Calculations. *ACS Cent. Sci.* **2021**, *7*, 467−475.
(34) Deshmukh, M. G.; Ippolito, J. A.; Zhang, C.-H.; Stone, E. A.; Reilly, R. A.; Miller, S. J.; Jorgensen, W. L.; Anderson, K. S. Structure-Guided Design of a Perampanel-Derived Pharmacophore Targeting the SARS-CoV-2 Main Protease. *Structure* **2021**, *29*, 823−833.
(35) Han, S. H.; Goins, C. M.; Arya, T.; Shin, W.-J.; Maw, J.; Hooper, A.; Sonawane, D. P.; Porter, M. R.; Bannister, B. E.; Crouch, R. D.; Lindsey, A. A.; Lakatos, G.; Martinez, S. R.; Alvarado, J.; Akers, W. S.; Wang, N. S.; Jung, J. U.; Macdonald, J. D.; Stauffer, S. R.

https://doi.org/10.1021/acs.jmedchem.1c01475
J. Med. Chem. XXXX, XXX, XXX−XXX

Structure-Based Optimization of ML300-Derived, Noncovalent Inhibitors Targeting the Severe Acute Respiratory Syndrome Coronavirus 3CL Protease (SARS-CoV-2 3CLpro). *J. Med. Chem.* **2021**, DOI: 10.1021/acs.jmedchem.1c00598.

(36) Kitamura, N.; Sacco, M. D.; Ma, C.; Hu, Y.; Townsend, J. A.; Meng, X.; Zhang, F.; Zhang, X.; Ba, M.; Szeto, T.; Kukuljac, A.; Marty, M. T.; Schultz, D.; Cherry, S.; Xiang, Y.; Chen, Y.; Wang, J. Expedited Approach toward the Rational Design of Noncovalent SARS-CoV-2 Main Protease Inhibitors. *J. Med. Chem.* **2021**, DOI: 10.1021/acs.jmedchem.1c00509.

(37) Zhu, L.; George, S.; Schmidt, M. F.; Al-Gharabli, S. I.; Rademann, J.; Hilgenfeld, R. Peptide Aldehyde Inhibitors Challenge the Substrate Specificity of the SARS-Coronavirus Main Protease. *Antiviral Res.* **2011**, *92*, 204−212.

(38) Dai, W.; Zhang, B.; Jiang, X.-M. M.; Su, H.; Li, J.; Zhao, Y.; Xie, X.; Jin, Z.; Peng, J.; Liu, F.; Li, C.; Li, Y.; Bai, F.; Wang, H.; Cheng, X.; Cen, X.; Hu, S.; Yang, X.; Wang, J.; Liu, X.; Xiao, G.; Jiang, H.; Rao, Z.; Zhang, L.-K. K.; Xu, Y.; Yang, H.; Liu, H. Structure-Based Design of Antiviral Drug Candidates Targeting the SARS-CoV-2 Main Protease. *Science* **2020**, *368*, 1331−1335.

(39) Zhang, L.; Lin, D.; Sun, X.; Curth, U.; Drosten, C.; Sauerhering, L.; Becker, S.; Rox, K.; Hilgenfeld, R. Crystal Structure of SARS-CoV-2 Main Protease Provides a Basis for Design of Improved α-Ketoamide Inhibitors. *Science* **2020**, *368*, 409−412.

(40) Clyde, A.; Galanie, S.; Kneller, D. W.; Ma, H.; Babuji, Y.; Blaiszik, B.; Brace, A.; Brettin, T.; Chard, K.; Chard, R.; Coates, L.; Foster, I.; Hauner, D.; Kertesz, V.; Kumar, N.; Lee, H.; Li, Z.; Merzky, A.; Schmidt, J. G.; Tan, L.; Titov, M.; Turilli, M.; Van Dam, H.; Chennubhotla, S. C.; Jha, S.; Kovalevsky, A.; Head, M.; Stevens, R. High Throughput Virtual Screening and Validation of a SARS-CoV-2 Main Protease Non-Covalent Inhibitor. *bioRxiv* **2021**, No. 2021.03.27.437323.

(41) Kneller, D. W.; Phillips, G.; Weiss, K. L.; Pant, S.; Zhang, Q.; O'Neill, H. M.; Coates, L.; Kovalevsky, A. Unusual Zwitterionic Catalytic Site of SARS-CoV-2 Main Protease Revealed by Neutron Crystallography. *J. Biol. Chem.* **2020**, *295*, 17365−17373.

(42) Kneller, D. W.; Phillips, G.; Weiss, K. L.; Zhang, Q.; Coates, L.; Kovalevsky, A. Direct Observation of Protonation State Modulation in SARS-CoV-2 Main Protease upon Inhibitor Binding with Neutron Crystallography. *J. Med. Chem.* **2021**, *64*, 4991−5000.

(43) Adamson, C. S.; Chibale, K.; Goss, R. J. M.; Jaspars, M.; Newman, D. J.; Dorrington, R. A. Antiviral Drug Discovery: Preparing for the next Pandemic. *Chem. Soc. Rev.* **2021**, *50*, 3647−3655.

(44) Pavlova, A.; Lynch, D. L.; Daidone, I.; Zanetti-Polzi, L.; Smith, M. D.; Chipot, C.; Kneller, D. W.; Kovalevsky, A.; Coates, L.; Golosov, A. A.; Dickson, C. J.; Velez-Vega, C.; Duca, J. S.; Vermaas, J. V.; Pang, Y. T.; Acharya, A.; Parks, J. M.; Smith, J. C.; Gumbart, J. Inhibitor Binding Influences the Protonation States of Histidines in SARS-CoV-2 Main Protease. *Chem. Sci.* **2021**, *12*, 1513−1527.

(45) Tummino, T. A.; Rezelj, V. V.; Fischer, B.; Fischer, A.; O'Meara, M. J.; Monel, B.; Vallet, T.; White, K. M.; Zhang, Z.; Alon, A.; Schadt, H.; O'Donnell, H. R.; Lyu, J.; Rosales, R.; McGovern, B. L.; Rathnasinghe, R.; Jangra, S.; Schotsaert, M.; Galarneau, J.-R.; Krogan, N. J.; Urban, L.; Shokat, K. M.; Kruse, A. C.; García-Sastre, A.; Schwartz, O.; Moretti, F.; Vignuzzi, M.; Pognan, F.; Shoichet, B. K. Drug-Induced Phospholipidosis Confounds Drug Repurposing for SARS-CoV-2. *Science* **2021**, *373*, 541−547.

(46) Dajnowicz, S.; Cheng, Y.; Daemen, L. L.; Weiss, K. L.; Gerlits, O.; Mueser, T. C.; Kovalevsky, A. Substrate Binding Stiffens Aspartate Aminotransferaseby Altering the Enzyme Picosecond Vibrational Dynamics. *ACS Omega* **2020**, *5*, 18787.

(47) Balog, E.; Becker, T.; Oettl, M.; Lechner, R.; Daniel, R.; Finney, J.; Smith, J. C. Direct Determination of Vibrational Density of States Change on Ligand Binding to a Protein. *Phys. Rev. Lett.* **2004**, No. 028103.

(48) Balog, E.; Perahia, D.; Smith, J. C.; Merzel, F. Vibrational Softening of a Protein on Ligand Binding. *J. Phys. Chem. B* **2011**, *115*, 6811−6817.

(49) Kingsley, L. J.; Brunet, V.; Lelais, G.; McCloskey, S.; Milliken, K.; Leija, E.; Fuhs, S. R.; Wang, K.; Zhou, E.; Spraggon, G. Development of a Virtual Reality Platform for Effective Communication of Structural Data in Drug Discovery. *J. Mol. Graphics Modell.* **2019**, *89*, 234−241.

(50) McCloskey, S.; Leija, E.; Hessenauer, S.; Funakawa, K. Nanome: Creating Powerful, Collaborative and Scientific VR Tools, 2020. Available from: https://nanome.ai.

(51) Bradley, D. M.; Branch, C. L.; Chan, W. N.; Couton, S.; Dean, A. W.; Doyle, P. M.; Evans, B.; Gilpin, M. L.; Gough, S. L.; Macritchie, J. A.; Marshall, H. R.; Nash, D. J.; Porter, R. A.; Ward, S. E. Acylated Piperidines as Glycine Transporter Inhibitors. US2008/0255144 A1, 2008.

(52) Kneller, D. W.; Phillips, G.; O'Neill, H. M.; Jedrzejczak, R.; Stols, L.; Langan, P.; Joachimiak, A.; Coates, L.; Kovalevsky, A. Structural Plasticity of SARS-CoV-2 3CL Mpro Active Site Cavity Revealed by Room Temperature X-Ray Crystallography. *Nat. Commun.* **2020**, *11*, No. 3202.

(53) Kneller, D. W.; Phillips, G.; Kovalevsky, A.; Coates, L. Room-Temperature Neutron and X-Ray Data Collection of 3CL Mpro from SARS-CoV-2. *Acta Crystallogr., Sect. F: Struct. Biol. Commun.* **2020**, *76*, 483−487.

(54) Luft, J. R.; Collins, R. J.; Fehrman, N. A.; Lauricella, A. M.; Veatch, C. K.; DeTitta, G. T. A Deliberate Approach to Screening for Initial Crystallization Conditions of Biological Macromolecules. *J. Struct. Biol.* **2003**, *142*, 170−179.

(55) Evans, P. R.; Murshudov, G. N. How Good Are My Data and What Is the Resolution? *Acta Crystallogr., Sect. D: Biol. Crystallogr.* **2013**, *69*, 1204−1214.

(56) Winn, M. D.; Ballard, C. C.; Cowtan, K. D.; Dodson, E. J.; Emsley, P.; Evans, P. R.; Keegan, R. M.; Krissinel, E. B.; Leslie, A. G. W. W.; McCoy, A.; McNicholas, S. J.; Murshudov, G. N.; Pannu, N. S.; Potterton, E. A.; Powell, H. R.; Read, R. J.; Vagin, A.; Wilson, K. S. Overview of the CCP4 Suite and Current Developments. *Acta Crystallogr., Sect. D: Biol. Crystallogr.* **2011**, *67*, 235−242.

(57) McCoy, A. J.; Grosse-Kunstleve, R. W.; Adams, P. D.; Winn, M. D.; Storoni, L. C.; Read, R. J. Phaser Crystallographic Software. *J. Appl. Crystallogr.* **2007**, *40*, 658−674.

(58) Adams, P. D.; Afonine, P. V.; Bunkóczi, G.; Chen, V. B.; Davis, I. W.; Echols, N.; Headd, J. J.; Hung, L. W.; Kapral, G. J.; Grosse-Kunstleve, R. W.; McCoy, A. J.; Moriarty, N. W.; Oeffner, R.; Read, R. J.; Richardson, D. C.; Richardson, J. S.; Terwilliger, T. C.; Zwart, P. H. PHENIX: A Comprehensive Python-Based System for Macromolecular Structure Solution. *Acta Crystallogr., Sect. D: Biol. Crystallogr.* **2010**, *66*, 213−221.

(59) Emsley, P.; Lohkamp, B.; Scott, W. G.; Cowtan, K. Features and Development of Coot. *Acta Crystallogr., Sect. D: Biol. Crystallogr.* **2010**, *66*, 486−501.

(60) Casañal, A.; Lohkamp, B.; Emsley, P. Current Developments in Coot for Macromolecular Model Building of Electron Cryo-Microscopy and Crystallographic Data. *Protein Sci.* **2020**, *29*, 1055−1064.

(61) Chen, V. B.; Arendall, W. B.; Headd, J. J.; Keedy, D. A.; Immormino, R. M.; Kapral, G. J.; Murray, L. W.; Richardson, J. S.; Richardson, D. C. MolProbity: All-Atom Structure Validation for Macromolecular Crystallography. *Acta Crystallogr., Sect. D: Biol. Crystallogr.* **2010**, *66*, 12−21.

(62) Moriarty, N. W.; Grosse-Kunstleve, R. W.; Adams, P. D. Electronic Ligand Builder and Optimization Workbench (ELBOW): A Tool for Ligand Coordinate and Restraint Generation. *Acta Crystallogr., Sect. D: Biol. Crystallogr.* **2009**, *65*, 1074−1080.

(63) Frisch, M. J.; Trucks, G. W.; Schlegel, H. B.; Scuseria, G. E.; Robb, M. A.; Cheeseman, J. R.; Scalmani, G.; Barone, V.; Petersson, G. A.; Nakatsuji, H.; Li, X.; Caricato, M.; Marenich, A. V.; Bloino, J.; Janesko, B. G.; Gomperts, R.; Mennucci, B.; Hratchian, H. P.; Ortiz, J. V.; Izmaylov, A. F.; Sonnenberg, J. L.; Williams-Young, D.; Ding, F.; Lipparini, F.; Egidi, F.; Goings, J.; Peng, B.; Petrone, A.; Henderson, T.; Ranasinghe, D.; Zakrzewski, V. G.; Gao, J.; Rega, N.; Zheng, G.; Liang, W.; Hada, M.; Ehara, M.; Toyota, K.; Fukuda, R.; Hasegawa, J.;

Ishida, M.; Nakajima, T.; Honda, Y.; Kitao, O.; Nakai, H.; Vreven, T.; Throssell, K.; Montgomery, J. A. J.; Peralta, J. E.; Ogliaro, F.; Bearpark, M. J.; Heyd, J. J.; Brothers, E. N.; Kudin, K. N.; Staroverov, V. N.; Keith, T. A.; Kobayashi, R.; Normand, J.; Raghavachari, K.; Rendell, A. P.; Burant, J. C.; Iyengar, S. S.; Tomasi, J.; Cossi, M.; Millam, J. M.; Klene, M.; Adamo, C.; Cammi, R.; Ochterski, J. W.; Martin, R. L.; Morokuma, K.; Farkas, O.; Foresman, J. B.; Fox, D. J. *Gaussian 16*, revision A.03; Gaussian Inc.: Wallingford, CT, 2016.

(64) Coates, L.; Cuneo, M. J.; Frost, M. J.; He, J.; Weiss, K. L.; Tomanicek, S. J.; McFeeters, H.; Vandavasi, V. G.; Langan, P.; Iverson, E. B. The Macromolecular Neutron Diffractometer MaNDi at the Spallation Neutron Source. *J. Appl. Crystallogr.* **2015**, *48*, 1302−1306.

(65) Coates, L.; Cao, H. B.; Chakoumakos, B. C.; Frontzek, M. D.; Hoffmann, C.; Kovalevsky, A. Y.; Liu, Y.; Meilleur, F.; dos Santos, A. M.; Myles, D. A. A.; Wang, X. P.; Ye, F. A Suite-Level Review of the Neutron Single-Crystal Diffraction Instruments at Oak Ridge National Laboratory. *Rev. Sci. Instrum.* **2018**, *89*, No. 092802.

(66) Coates, L.; Sullivan, B. The Macromolecular Neutron Diffractometer at the Spallation Neutron Source. *Neutron Crystallography in Structural Biology*; Methods in Enzymology; Academic Press Inc., 2020; Vol. *634*, pp 87−99.

(67) Sullivan, B.; Archibald, R.; Langan, P. S.; Dobbek, H.; Bommer, M.; Mcfeeters, R. L.; Coates, L.; Wang, X.; Gallmeier, F.; Carpenter, J. M.; Lynch, V.; Langan, P. Improving the Accuracy and Resolution of Neutron Crystallographic Data by Three-Dimensional Profile Fitting of Bragg Peaks in Reciprocal Space. *Acta Crystallogr., Sect. D: Struct. Biol.* **2018**, *74*, 1085−1095.

(68) Campbell, J. W.; Hao, Q.; Harding, M. M.; Nguti, N. D.; Wilkinson, C. LAUEGEN Version 6.0 and INTLDM. *J. Appl. Crystallogr.* **1998**, *31*, 496−502.

(69) Adams, P. D.; Mustyakimov, M.; Afonine, P. V.; Langan, P. Generalized X-Ray and Neutron Crystallographic Analysis: More Accurate and Complete Structures for Biological Macromolecules. *Acta Crystallogr., Sect. D: Biol. Crystallogr.* **2009**, *65*, 567−573.

(70) Mustyakimov, M.; Langan, P. *NCNS: An Open Source Distribution Patch for CNS for Macromolecular Structure Refinement*; Los Alamos National Security: Los Alamos, NM, 2007.

(71) Kuo, C. J.; Chi, Y. H.; Hsu, J. T. A.; Liang, P. H. Characterization of SARS Main Protease and Inhibitor Assay Using a Fluorogenic Substrate. *Biochem. Biophys. Res. Commun.* **2004**, *318*, 862−867.

(72) Kneller, D. W.; Galanie, S.; Phillips, G.; O'neill, H. M.; Coates, L.; Kovalevsky, A. Malleability of the SARS-CoV-2 3CL Mpro Active-Site Cavity Facilitates Binding of Clinical Antivirals. *Structure* **2020**, *28*, 1313−1320.

(73) Bocci, G.; Bradfute, S. B.; Ye, C.; Garcia, M. J.; Parvathareddy, J.; Reichard, W.; Surendranathan, S.; Bansal, S.; Bologa, C. G.; Perkins, D. J.; Jonsson, C. B.; Sklar, L. A.; Oprea, T. I. Virtual and in vitro antiviral screening revive therapeutic drugs for COVID-19. *ACS. Pharmacol. Transl. Sci.* **2020**, *3*, 1278−1292.

https://doi.org/10.1021/acs.jmedchem.1c01475
J. Med. Chem. XXXX, XXX, XXX−XXX